Master's Thesis

Excitability and Memory in a Time-Delayed Optoelectronic Neuron

submitted by

Jonas Mayer Martins

supervised by

Svetlana V. Gurevich
Julien Javaloyes

University of Münster
Institute for Theoretical Physics

March 1, 2024

Declaration of Academic Integrity

I hereby confirm that this thesis on *Excitability and Memory in a Time-Delayed Optoelectronic Neuron* is solely my own work and that I have used no sources or aids other than the ones stated. All passages in my thesis for which other sources, including electronic media, have been used, be it direct quotes or content references, have been acknowledged as such and the sources cited.

March 1, 2024 

I agree to have my thesis checked in order to rule out potential similarities with other works and to have my thesis stored in a database for this purpose.

March 1, 2024 

Contents

I declare that this thesis has been published by the author as an article [46]. In particular, Sections 1, 2.3, and 3-5 consist almost exclusively of sections that were published in this article. Only the theoretical introduction in Section 2, except Section 2.3, is unpublished and has been written explicitly for this thesis.

1 Introduction

The human brain is arguably the most exciting matter in the universe. Consuming as little power as a light bulb, the brain is extremely power-efficient and still outperforms artificial computers in many ways [12]. The vast majority of modern-day computers implement the von Neumann architecture [78]. Considering the scientific, technological and socio-cultural progress that computers have bestowed upon us [31], the classical computing architecture has served us well. Yet with the ever-increasing demand for higher computing power and the advent of artificial intelligence, major issues have become apparent. First, classical computers encode information digitally, which entails high energy consumption, primarily due to heat dissipation (the information and communication technology (ICT) sector accounts for around 2 % to 4 % of the global greenhouse gas emissions, of which only 23 % are embodied emissions [18]). Second, the CPU processes information sequentially, limiting bandwidth. Furthermore, the physical distance between computational units slows down computation even further. Last, the size of transistors, which primarily drives Moore's law, is limited by quantum effects [76].

The answer to these challenges might be to mimic the brain. So-called *neuromorphic computing* emulates the structure of the brain by connecting artificial neurons in a network, thus merging memory and processing units [44]. Neuromorphic computing is particularly suited for implementing integrated machine learning algorithms [70]. A multitude of electronic excitable systems have been studied as potential candidates for artificial neurons and tested experimentally on neuromorphic chips, e.g., Neurogrid [4], TrueNorth [48], as well as SpiNNaker [19] and FACETS [65] as part of the Human Brain Project [45, 38]. Electronic artificial neurons, however, are relatively slow (kHz) and suffer from heat loss due to dissipation in electric interconnects, which makes them energy-intensive (pJ/spike) [49]. Conversely, optical computing promises high computing speeds at extremely low energy costs [9, 16, 70]. Optical

or optoelectronic artificial neurons have been implemented, for example, as a semiconductor ring laser [11], graphene excitable laser [69], time-delayed optoelectronic resonator [63], and vertical-cavity surface-emitting laser (VCSEL) [43, 29]. Miniaturization of the devices is another avenue to further increase efficiency. Although smaller sizes come with challenges associated with the diffraction limit and other quantum effects, such as the Purcell effect [62], nanoscale devices, e.g., semiconductor lasers, promise high speed and require little power [30, 40].

In this thesis, we study a system consisting of a *resonant-tunneling diode* (RTD) driving a *laser diode* (LD) subjected to time-delayed feedback. Both the RTD and the LD can be of nanoscopic scale in our model. We derive the stochastic delay-differential equations (DDEs) that describe the combined RTD-LD system from Ref. [57], where this system has been shown numerically to be excitable and propagate pulses from one neuron to another.

We perform a comprehensive theoretical analysis using a combination of time simulations and path-continuation methods to determine how the RTD-LD can function as an artificial neuron. Most importantly, we shall demonstrate that our model exhibits TLSs as solutions and discuss under which conditions the paradigmatic FHN model, which was employed in an earlier theoretical study of the RTD-LD [63] and neglected the laser dynamics through an adiabatic approximation and Pyragas-type feedback [60, 66], is justified. We show that the DDE model employed here qualitatively reproduces the delayed FHN model in a limiting case, yet exhibits new features and challenges – multistability of TLSs and instability of multi-pulse states due to attractive interaction forces – that arise due to the nanoscale laser.

This thesis is structured as follows: First, we provide some theoretical background on bifurcation analysis and neural models in Section 2. In Section 3, we introduce the DDEs that model the RTD-LD along with the numerical methods. Subsequently, we analyze the system by combining time simulations and path continuation methods in Section 4. This analysis consists of four main parts: a brief overview of the RTD without feedback (as studied in Ref. [56]) in Section 4.1, then the RTD-LD subject to feedback with a slow RTD in Section 4.2 and a fast RTD in Section 4.3 as well as a discussion of the characteristic time scale connecting these two regimes in Section 4.4. Finally, we discuss our results, in particular the impact of the RTD time scale on the memory properties of the system and hence its viability as an artificial neuron, and give an outlook in Section 5.

2 Dynamical systems and neural models

2.1 Bifurcations and stability analysis

An important class of dynamical systems, where a system state $\vec{x}$ changes over time t, can be modeled by time-continuous vector fields described by *ordinary differential equations* (ODEs)

$$\dot{x} = f(x, t; \mu) \tag{2.1}$$

or time-discrete *maps*

$$x \mapsto g(x; \mu)\,, \tag{2.2}$$

where the state is an n-dimensional vector $x \in \mathbb{R}^n$, time is a scalar $t \in \mathbb{R}$, and the p-dimensional parameter is $\mu \in \mathbb{R}^p$. In this introduction, which is based primarily on the classic textbooks by Argyris [2], Strogatz [72], and Wiggins [80], we shall focus on continuous maps. In fact, we only need to consider systems of *first-order* ODEs because higher-order derivatives can be recast as additional dimensions, for example, $\ddot{x} = x$ is equivalent to $\dot{x}_1 = x_2$ and $\dot{x}_2 = x_1$. Explicit time dependence is dealt with by setting $x_{n+1} = t$, such that $\dot{x}_{n+1} = 1$. The ODEs we are interested in are thus of the form

$$\dot{x} = f(x; \mu)\,. \tag{2.3}$$

Since most ODEs cannot be solved analytically, we must resort to numerical and qualitative means of analysis. In particular, there are two main questions about a dynamical system that we seek to answer: First, what is its long-term behavior? Second, if we change the parameters μ, are there tipping points, where the long-term behavior changes fundamentally? A state $\bar{x}$ is an equilibrium solution – variously called a *fixed point*, *singular point*, or *steady state*[1] – if it does not change over time, that is,

$$\dot{\bar{x}} = f(\bar{x}) = 0\,. \tag{2.4}$$

We omit the explicit dependence on the parameters μ here and in the following.

The stability of the fixed point $\bar{x}$ is determined by whether small perturbations $\delta = x - \bar{x}$

[1] Let us remark that the field of nonlinear dynamics and complex systems has not yet converged to a common terminology and usage of names for related or unrelated concepts is at times conflicting [34, pp. 208].

grow or shrink and can therefore be obtained by linearizing system (2.3) through a Taylor expansion to first order in δ about the fixed point $\bar{x}$,

$$\dot{\delta} = \dot{x} = f(\bar{x}) + Df(\bar{x})\delta + \mathcal{O}(|\delta|^2)\,, \tag{2.5}$$

where Df is the derivative of f. Since $\bar{x}$ is a fixed point, $\dot{\bar{x}} = f(\bar{x}) = 0$. In the vicinity of the fixed point, the higher order terms $\mathcal{O}(|\delta|^2)$ can be neglected if the linear stability analysis is unambiguous – we shall discuss later what this means precisely. We are therefore concerned with the linear system

$$\dot{\delta} = Df(\bar{x})\delta \tag{2.6}$$

to understand how perturbations of the fixed point evolve. To solve Eq. (2.6) with a time-dependent coefficient matrix $Df(x(t))$ would be daunting because there is no general analytical solution, but since we are only interested in the equilibrium state $\delta = 0$, where $x(t) = \bar{x}$ is constant, system (2.6) is easily solved by the matrix exponential,

$$\delta(t) = \delta_0 \mathrm{e}^{Df(\bar{x})t}\,, \tag{2.7}$$

with the initial condition $\delta(0) = \delta_0$. The solution $\delta = 0$ and $x = \bar{x}$ is therefore asymptotically stable if all eigenvalues of $Df(\bar{x})$ are negative since this implies that small perturbations relax back to equilibrium, $\lim_{t\to\infty} \delta(t) \to 0$. Conversely, it is unstable if at least one eigenvalue is positive.

The question remains under which circumstances the linear stability analysis is valid to describe the nonlinear stability of an equilibrium. According to the Hartman-Grobman theorem, the local phase space of an equilibrium solution is topologically the same as the phase space of the linearized system if the fixed point is *hyperbolic* or *non-degenerate*, that is, the spectrum of $Df(\bar{x})$ contains no eigenvalues with zero real part [24, 27, 28]. This theorem implies that the stability of the solution $\delta = 0$ to Eq. (2.6) is indeed the same as the stability of the fixed point $\bar{x}$. If, on the other hand, a fixed point is *non-hyperbolic* or *degenerate*, small perturbations can change the phase space qualitatively. Higher order terms must be taken into account to determine the stability of a non-hyperbolic fixed point if there are no eigenvalues with positive real part. Note that non-hyperbolicity is necessary but not

sufficient for a bifurcation of fixed points to occur. As pointed out in Ref. [80, pp. 361], for example, the flow of the vector field $f(x) = \mu - x^3$, even though $x = 0$ is non-hyperbolic since $f'(0)|_{\mu=0} = 0$, is qualitatively the same for $\mu < 0$ and $\mu > 0$ because there is just one stable fixed point defined by $x = \mu^{1/3}$.

The eigenvalues of Df are immensely important to understand the dynamics of a system. Every eigenvalue describes the stability of an invariant manifold in the phase space that aligns locally with the direction of the eigenvectors. A manifold with eigenvalue zero is called a *center manifold*. If by varying the control parameter μ an eigenvalue crosses the imaginary axis, the stability of such a manifold changes, which means that the topology of the phase space changes as well. Such qualitative changes of the dynamics are called *bifurcations*. If they can be described locally through a linearized system, they are *local* bifurcations and they can be reduced to a canonical representation of the respective bifurcation, the *normal form*. Otherwise, they are *global* bifurcations, which can be more difficult to detect and analyze.

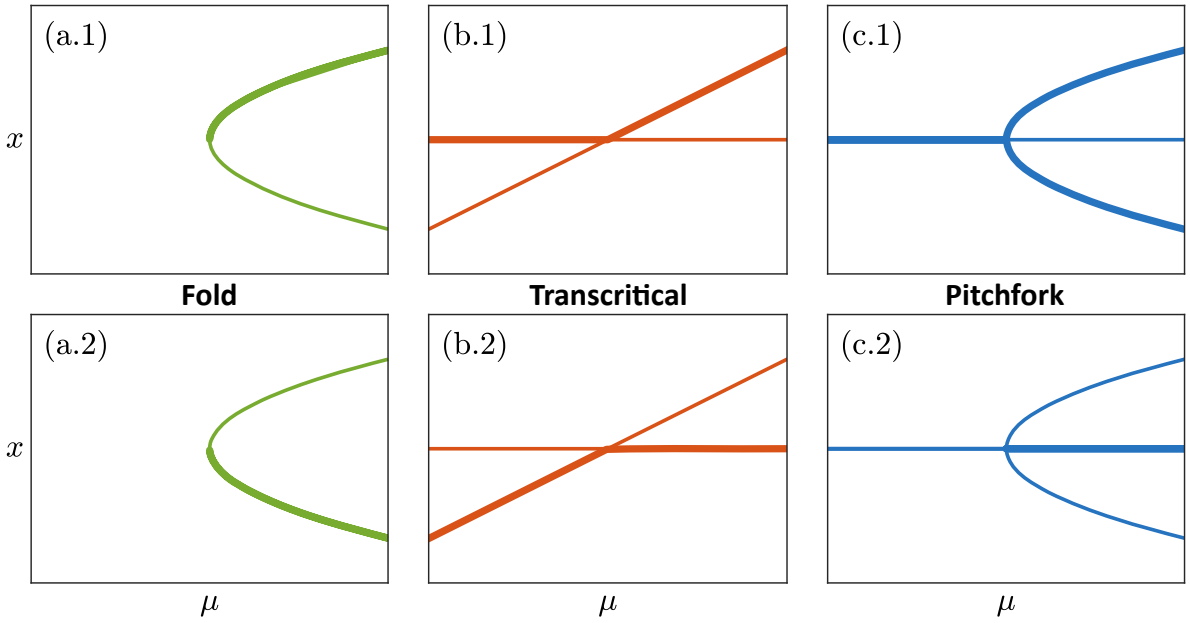

Figure 2.1: Bifurcations of fixed points: (a) Fold, (b) transcritical, and (c) pitchfork bifurcations.

Bifurcations of fixed points There are just three codimension-1 bifurcations of fixed points, which arise by changing a one-dimensional bifurcation parameter μ, illustrated in Fig. 2.1.

Each bifurcation comes in two different types, depending on a sign change in the normal form. Panel (a) shows a *fold*, *tangent*, or *saddle-node* bifurcation with the normal form

$$(1) \quad f(x) = \mu - x^2 \,, \quad (2) \quad f(x) = -\mu + x^2 \,. \tag{2.8}$$

In panel (b), the *transcritical* bifurcation has the normal form

$$(1) \quad f(x) = \mu x - x^2 \,, \quad (2) \quad f(x) = -\mu x + x^2 \,. \tag{2.9}$$

Panel (c) shows a pitchfork bifurcation with the normal form

$$(1) \quad f(x) = \mu x - x^3 \,, \quad (2) \quad f(x) = -\mu x + x^3 \,. \tag{2.10}$$

Bifurcations of periodic solutions So far, we have only considered steady states. Periodic solutions require a more sophisticated approach to determine their stability: With the help of a *Poincaré section*, the dynamics of the periodic solution can be reduced to a *Poincaré map* or *first-return map*, which maps the intersections of the periodic orbit with the Poincaré section from on period to the next. Mathematically, this means that we define an $(n-1)$–dimensional hypersurface Σ in $\mathbb{R}^n$ that is transversal to the trajectory. The intersection points $P^{(0)}$, $P^{(1)}$, $P^{(2)}$, etc. will then be described by a map g from one period i to the next period $i+1$,

$$P^{(i+1)} = g(P^{(i)}) \,. \tag{2.11}$$

To illustrate these concepts, consider the Lorenz system [39], developed by Edward Lorenz together with Ellen Fetter and Margaret Hamilton to model atmospheric convection,

$$\begin{aligned} \dot{X} &= \sigma(Y - X) \\ \dot{Y} &= X(r - Z) - Y \\ \dot{Z} &= XY - bZ \end{aligned} \tag{2.12}$$

in Fig. 2.2 with $\sigma = 10$ and $b = 8/3$. Panel (a) shows the phase space, where we compare a limit cycle at $r = 160$ in red and a strange attractor at $r = 167$ in blue. The Poincaré section in peach lies at $Y = 0$. This panel is a stereogram, so you can see the figure as a three-dimensional

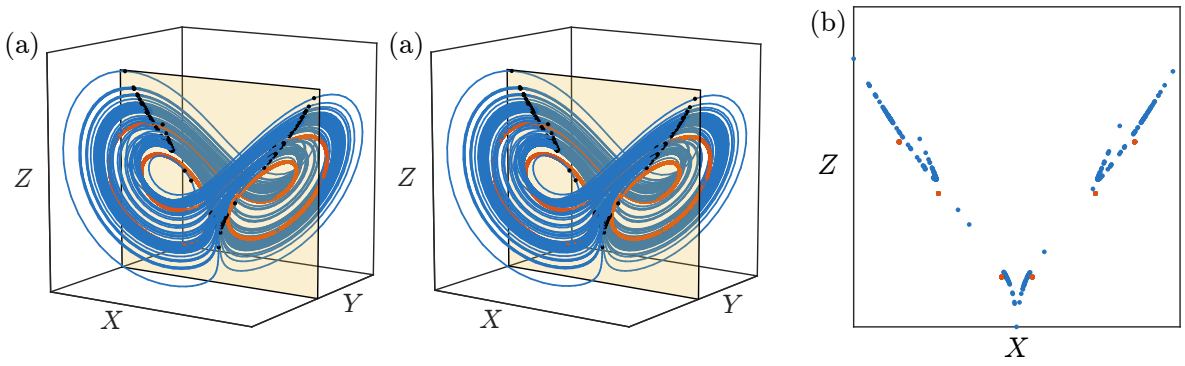

Figure 2.2: (a) Stereogram of the Lorenz system with a limit cycle (red) at $r = 160$, a strange attractor (blue) at $r = 167$ and a Poincaré section (peach), along with (b) the corresponding Poincaré map.

object by looking into the far field and then superimposing the disparate images of each eye until the middle pair of the four images aligns. This technique is called the *magic eye* and can be easily produced for any three-dimensional object by rotating the figure by a small angle to emulate the different perspective of each eye. Panel (b) shows the Poincaré map of the two solutions, from which we see that the limit cycle is characterized by six distinct points that repeat with each period, whereas the strange attractor forms a manifold because it is aperiodic.

In the coordinate system of the Poincaré section with position vector ξ, we can then analyze the stability of this map g to deduce the stability of the periodic orbit. Similar to the discussion of flows above, the stability of a perturbation $\delta = \xi - \bar{\xi}$ of a fixed point $\bar{\xi}$ is defined by

$$\eta^{(i+1)} = Dg(\bar{\xi})\eta^{(i)}\,, \tag{2.13}$$

where Dg is the derivative of g. Hence, the spectrum of $Dg(\bar{\xi})$ determines the stability, but the critical manifold is not the imaginary axis as it is for flows but the unit circle. For if an eigenvalue λ, also referred to as *Floquet multiplier*, has a magnitude $|\lambda| < 1$, the perturbation dies away and the corresponding invariant manifold of the map g is stable; if $|\lambda| > 1$, the manifold is unstable; and if $|\lambda| = 1$, it is a center manifold. The Floquet multipliers satisfy

$$\lambda^k(T) = \lambda(kT) \tag{2.14}$$

for $k \in \mathbb{N}$, that is, the eigenvalues of the Poincaré map for k periods T are the same as the as k times the eigenvalues of the Poincaré map for one period T. This relation implies that the Floquet multipliers are of the form

$$\lambda(T) = \mathrm{e}^{\sigma T}\,, \tag{2.15}$$

where σ are the *Floquet exponents*. Analogously to steady state bifurcations, when an

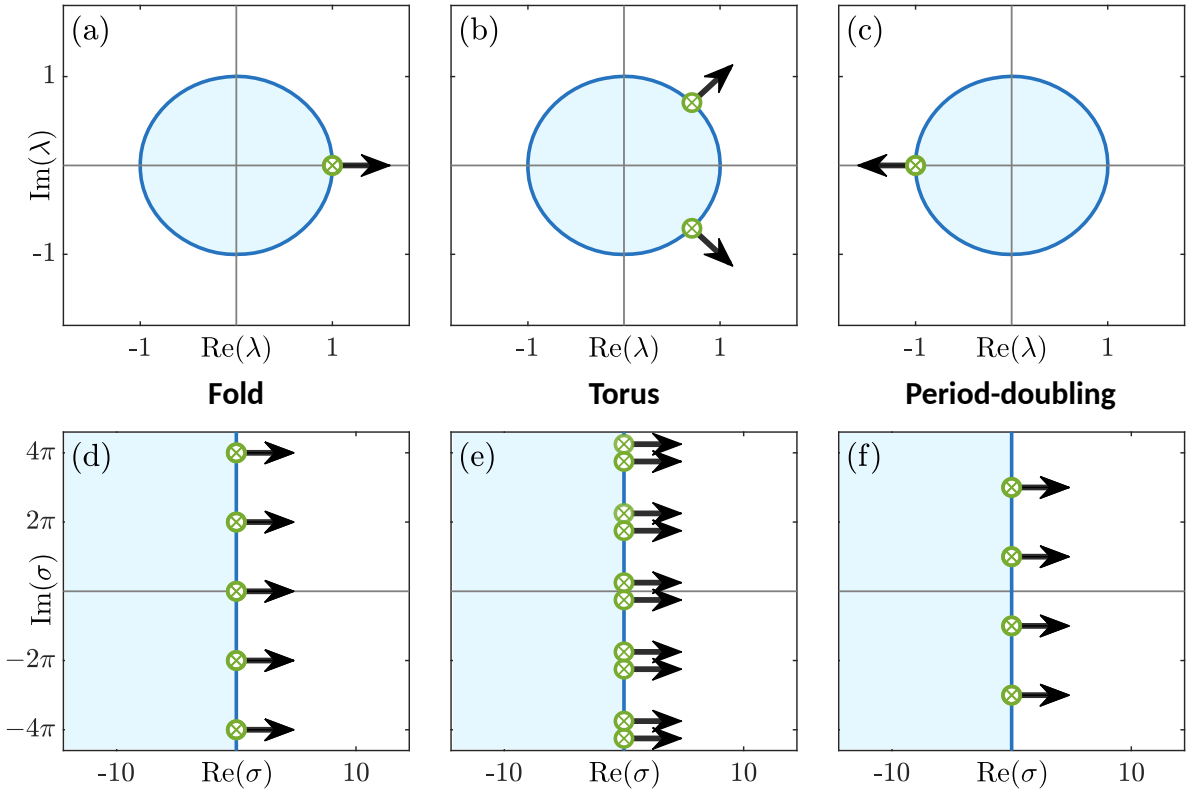

Figure 2.3: Motion of the (a-c) Floquet multipliers and (d-f) Floquet exponents during local periodic bifurcations: (a, d) Fold, (b, e) torus, and (c, f) period-doubling bifurcation. The stable region is colored blue.

invariant manifold changes its stability because the associated eigenvalue crosses the unit circle, a bifurcation occurs. There are three ways how a periodic solution can lose its stability, as illustrated in Fig. 2.3 for the Floquet multipliers (a-c) and the Floquet exponents (d-f): A *fold bifurcation* of limit cycles occurs if a real Floquet multiplier crosses 1, see panels (a) and (d). A *torus bifurcation* occurs if a pair of complex conjugate Floquet multiplier crosses the unit circle, see panels (b) and (e). This bifurcation, which manifests itself as a *Neimarck-Sacker*

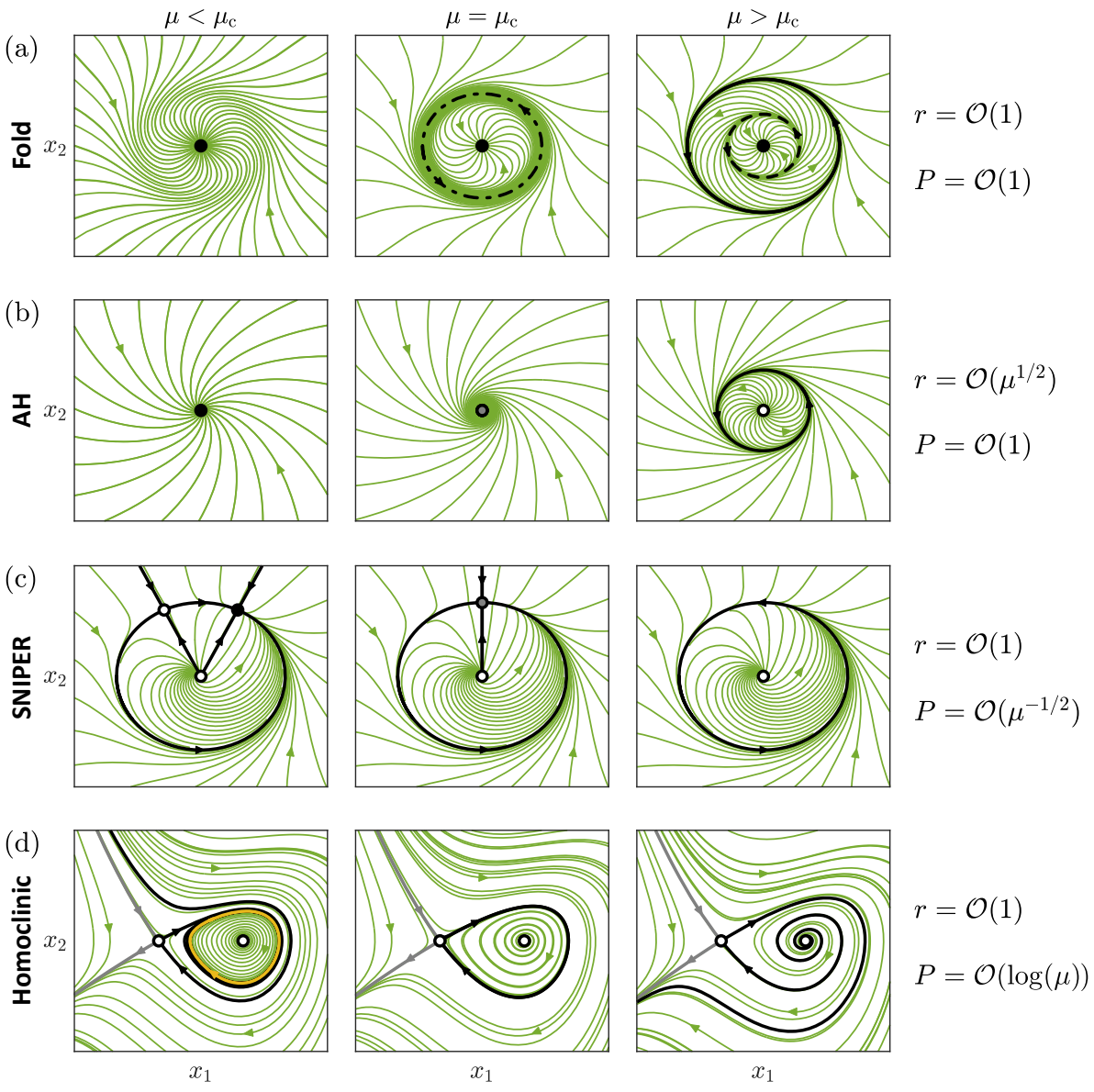

Figure 2.4: Periodic bifurcations: (a) fold, (b) Andronov-Hopf (AH), (c) Saddle-node infinite-period (SNIPER), and (d) homoclinic bifurcation.

bifurcation of the Poincaré map, adds another periodicity and can lead to quasi-periodic solutions branching off. Third, a *period-doubling* or *flip bifurcation* occurs if a real Floquet multiplier crosses the unit circle at -1.

A selection of codimension-1 bifurcations leading to periodic solutions is depicted in Fig. 2.4. In panel (a), we see that a fold bifurcation emerges as a limit cycle appearing "out of the blue sky" at the critical bifurcation parameter value μ_c and separating into a stable and an unstable limit cycle. The radius r and the period P do not depend on the bifurcation parameter μ. Next, in panel (b), a stable limit cycle emerges from a stable fixed point with the latter losing its stability because two complex conjugate eigenvalues cross the imaginary axis. This is a *supercritical Andronov-Hopf (AH) bifurcation*. In a *subcritical* AH, the stability is inverted. The period of this limit cycle does not scale with the bifurcation parameter, but the radius is of order $O(\mu^{1/2})$. In panel (c), the *saddle-node infinite-period bifurcation* is a saddle-node (or fold) of fixed points occurring on a limit cycle. Finally, in panel (d), the *homoclinic bifurcation* is a limit cycle colliding with a fixed point. A homoclinic orbit is a trajectory connecting a fixed point to back to itself. Likewise, a heteroclinic orbit fixed point is a trajectory between two different fixed points. These orbits are created by a collision of an unstable and a stable invariant manifold. The SNIPER and homoclinic bifurcations are global bifurcations and they can be distinguished by the scaling of their period as $P = O(\mu^{-1/2})$ for the SNIPER and $P = O(\log(\mu))$ for the homoclinic bifurcation.

2.2 Delay-differential equations

Many physical systems can be modeled successfully by ordinary differential equations (ODEs), time-discrete maps, or partial differential equations (PDEs). The former two describe the temporal evolution of finite-dimensional variables, whereas the latter are infinite-dimensional and are often employed to study how spatially extended systems evolve over time. Another important class of models, the *delay-differential equations* (DDEs), generalize ODEs to account for time lags. With a single constant time delay τ, a DDE has the form,

$$\dot{x} = f(x(t), x(t-\tau)) \,, \tag{2.16}$$

where the initial conditions need to be defined for $t \in [\tau, 0)$. However, keep in mind that DDEs can have arbitrarily many, variable time delays. From the fact that we need to define the infinitely many initial conditions on a continuous interval, we see that DDEs are generally infinitely-dimensional. Moreover, there is a deep relation between DDEs and PDEs, for the strictly temporal dynamics can resemble the evolution of a spatial domain in the *two-time* representation to be discussed below [81]. To account for the delay and the resulting pseudo-continuous spectrum of the eigenvalues in the stability analysis, the methods to analyze differential equations need to be adapted. For example, we use DDE-BifTool [14] for numerical path-continuation. A mathematical introduction based on the more general concept of functional differential equations, where DDEs are called *retarded* functional differential equations is given in Ref. [26]. For a more applied perspective, consult Refs. [15] and [81].

2.3 Neurons and excitability

An essential property of neurons allowing them to process and transmit information is *excitability* [21]. From a dynamical systems perspective [33, 34], a system is excitable if a sufficiently strong perturbation of the resting state elicits a large-amplitude excursion in phase space that is largely independent of the details of the perturbation and subsequently returns to the resting state.

For neurons, this large-amplitude response of the membrane potential is called an *action potential*, *pulse*, or *spike*. Excitability is a ubiquitous concept, not only in biology [52, 53, 61] but also in chemistry, e.g., the Belousov–Zhabotinsky reaction [36, 52], and in physics, e.g., lasers [68, 69], particles trapped in an optical torque wrench [58], and resonant-tunneling diodes (RTDs) [64]. There are, in fact, just four generic types of excitability, defined by the nearby codimension-1 bifurcations that lead to a limit cycle [34]. In Fig. 2.5, these routes to excitability are illustrated with the *Morris–Lecar model* of biological neurons, originally proposed to model voltage patterns of barnacle giant muscle fibers [50]. Let us briefly introduce this model before discussing the types of excitability.

To model how the voltage V across a neuron membrane reacts to an excitatory current I, the Morris–Lecar model takes into account the current flow through the Ca^{2+} and K^+ chan-

nels in the neuronal membrane with capacitance C, and an additional leakage current of ions diffusing directly through the membrane. These ionic currents are proportional to the deviation of the voltage from their respective resting potentials V_{Ca}, V_{K}, and V_{L}, the maximum conductances g_{Ca}, g_{K}, and g_{L}, as well as the opening probabilities m_∞ and w of the Ca^{2+} and K^+ channels, respectively. The model is therefore

$$C\dot{V} = I - \overline{g}_{\mathrm{Ca}} m_\infty (V - V_{\mathrm{Ca}}) - \overline{g}_{\mathrm{K}} w (V - V_{\mathrm{K}}) - \overline{g}_{\mathrm{L}} (V - V_{\mathrm{L}}) \,, \tag{2.17}$$

$$\dot{w} = \frac{w_\infty - w}{\tau_w} \,, \tag{2.18}$$

with equilibrium activation functions

$$m_\infty = \frac{1}{2}\left[1 + \tanh\left(\frac{V - V_1}{V_2}\right)\right], \tag{2.19}$$

$$w_\infty = \frac{1}{2}\left[1 + \tanh\left(\frac{V - V_3}{V_4}\right)\right], \tag{2.20}$$

and time constant

$$\tau_w = \left[\phi \cosh\left(\frac{V - V_3}{2V_4}\right)\right]^{-1}, \tag{2.21}$$

where ϕ is a temperature scaling factor. We determined the parameter values used in Fig. 2.5 from the bifurcation analysis of the Morris–Lecar equations in Ref. [74]. The fixed parameters are listed in Table 1.

Table 1: Parameters of the Morris–Lecar model in panels (a)-(d) of Fig. 2.5. The voltages are given in units of mV, the conductances in $\mathrm{mS\,cm^{-2}}$, and the capacitances in $\mu\mathrm{F\,cm^{-2}}$. Varied parameters are violet.

Case	C	I	V_1	V_2	V_3	V_4	V_{Ca}	V_{K}	V_{L}	g_{Ca}	g_{K}	g_{L}	ϕ
(a)	20	{35, 39.8, 70}	-1.2	18	12	17.4	120	-80	-60	4	8	2	1/15
(b)	20	{35, 39.8, 42}	-1.2	18	12	17.4	120	-80	-60	4	8	2	1/5
(c)	20	{35, 60, 130}	-1.2	18	2	17.4	120	-80	-60	2.4	8	2	1/15
(d)	20	{43, 50.5, 55}	-1.2	18	2	17.4	120	-80	-60	4	8	2	1/15

In Fig. 2.5, we show the phase space (V, w) and the nullclines $\dot{V} = 0$ (red) and $\dot{w} = 0$ (yellow). The fixed points defined by intersection of the nullclines are indicated by white circles. The green lines are exemplary trajectories in the phase space to visualize to phase flow. The blue trajectory is the result of a perturbation (white star) of the steady state that

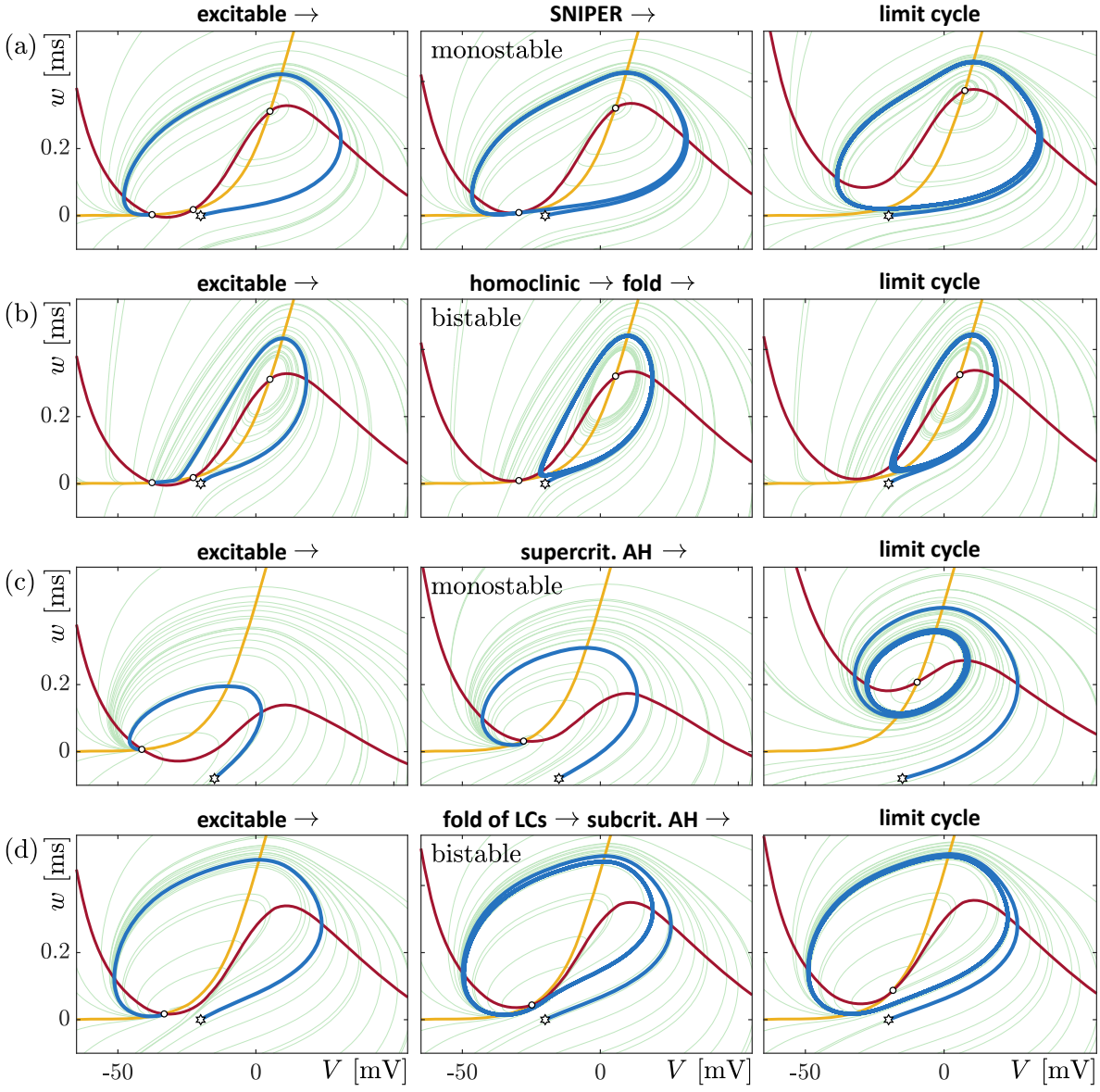

Figure 2.5: The four paths from excitability to limit cycles via (a) a SNIPER, (b) homoclinic and fold, (c) a supercritical AH, and (d) a fold of limit cycles and a subcritical AH bifurcation. The parameters of the Morris–Lecar model shown here are listed in Table 1. The green lines are trajectories, the blue line is an excited trajectory starting from a perturbation of a steady state at the star. The nullclines $\dot{V} = 0$ (red) and $\dot{w} = 0$ (yellow) define fixed points (white circles).

results in a large-amplitude excursion in phase space. The system is excitable on the left of each panel because it is located close to a bifurcation or set of bifurcations that lead to a limit cycle. In panel (a), this bifurcation is a SNIPER, where a stable and unstable fixed point merge in a fold on an invariant manifold that becomes the limit cycle. In panel (b), the sequence is a homoclinic followed by a fold bifurcation. In panel (c), a supercritical AH bifurcation leads to a limit cycle emerging from the single fixed point. This route to excitability is least pronounced in the Morris–Lecar model. Finally, in panel (d), two limit cycles emerge from a fold of limit cycles and subsequently, the unstable of those two limit cycles disappears in a subcritical AH bifurcation. While the limit cycle of the SNIPER and supercritical AH in panels (a) and (c) is monostable close to the excitable region in phase space, the route in panel (b) is bistable in the sense that the limit cycle and the fixed point involved in these bifurcations remain stable between the homoclinic and the fold, as is also the case in panel (d) between the two bifurcations.

Historically, the excitability types have been classified by the scaling of the frequency at which action potentials are generated depending on the strength of the applied current [34, 59]: type I neurons are continuous in frequency (because the period starts at infinity), whereas type II have a jump in frequency. From the perspective of nonlinear dynamics, this classification is not very enlightening since type I is a SNIPER bifurcation and type II the rest, i.e., an AH or a fold next to a limit cycle.

The combination of excitability and delay is known to give rise to *temporal localized states* (TLSs) in many systems, such as in a semiconductor laser with coherent optical injection [20, 51], the FHN neuron with delayed feedback [63, 82], and the Morris–Lecar model of biological neurons [50, 74, 71]. Since TLSs are self-healing in the sense that these solutions are robust to perturbations, they can encode information and act as memory. The FitzHugh–Nagumo (FHN) model is a prototypical model of excitability [8, 34, 37, 83, 42, 43] and has been used, in particular, to model the RTD-LD. Let us briefly discuss the features most important for our subsequent analysis, especially the emergence of TLSs in the delayed FHN model presented in Ref. [63].

The differential equations of the FHN model [35],

$$\dot{v} = f(v) - i + \alpha \,, \tag{2.22}$$

$$\dot{i} = \varepsilon(v_0 + v - ri) \,, \tag{2.23}$$

describe the evolution of the voltage v and current i. In Eq. (2.22), α is the stimulus current and the current-voltage characteristic $f(v) = v - v^3/3$ defines the steady state of i if $\alpha = 0$. In Eq. (2.23), the resistance is r, the bias voltage is v_0, and the stiffness ε relates to the ratio of the timescales of the two state variables v and i. The Van-der-Pol oscillator is the special case $v_0 = r = 0$ and the FHN model is itself a simplified version of the Hodgkin-Huxley neuron model [32].

In Ref. [63], the delayed FHN model

$$\dot{v} = f(v) - i + \kappa[i(t-\tau) - i] \,, \tag{2.24}$$

$$\dot{i} = \varepsilon(v_0 + v) \tag{2.25}$$

replaces the stimulus current α by a feedback with time delay τ and feedback strength κ. Furthermore, the resistance is $r = 0$ to obtain a vertical load line defining the steady state at v_0, thus avoiding bistable steady state solutions. Typical values used in Ref. [63] and here are $\varepsilon = 0.05$, $\kappa = 0.18$, and $\tau = 500$. The time-delayed feedback in the delayed FHN model is of Pyragas type [66], i.e., of the form $i(t-\tau) - i(t)$. A property of this type of feedback, used also in chaos control, is that it is non-invasive, that is, it has no influence on the steady state.

Figure 2.6 shows the FHN model without feedback ($\kappa = 0$). The current-voltage characteristic $f(v) = v - v^3/3$ (blue) defines the nullcline $\dot{v} = 0$ and its intersection with the vertical nullcline $\dot{i} = 0$ at the bias voltage $v = -v_0$ defines the steady state i_{st}. In panel (a), we show periodic orbits in the phase space (v, i) that exist for a range of bias voltages, $v_0 \in [-1, 1]$. The bifurcation diagram in panel (b) depicts how the periodic orbit solution emerges from the steady state, which loses its stability in an AH bifurcation at $v_0 = 1$. Here and in the following, we use the integrated intensity over one period T,

$$\langle x \rangle = \frac{1}{T} \int_0^T \mathrm{d}t \, x(t) \,, \tag{2.26}$$

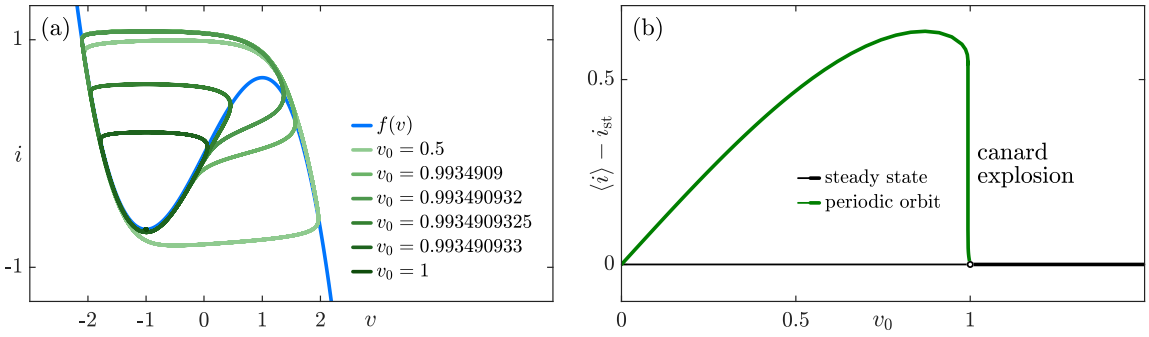

Figure 2.6: Canard in the FHN model without delayed feedback: (a) phase space (v, i) and bifurcation diagram in the bias voltage v_0 showing a sudden increase in the amplitude of the periodic solution around $v_0 = 1$. Thick lines indicate stable solutions.

as measure for periodic solutions.

The sudden increase in the amplitude of the limit cycle around the bifurcation points indicates a *canard explosion* [79]. First discovered in 1981 [5], the canard is a rapid transition from small-amplitude to large-amplitude limit cycles by varying a control parameter in an exponentially narrow range [34]. Canards are associated with excitable systems such as neurons [13, 64, 84, 56, 23] but also orgasms [6], where they can induce quasi-thresholds. We shall see below that the RTD-LD is excitable due to a canard as well. This is the route to excitability via a fold of limit cycles and a subcritical Hopf illustrated in Fig. 2.5 (d).

Now, let us consider the FHN model *with* time-delayed feedback, $\kappa > 0$, as illustrated in Fig. 2.7. This figure is motivated by the bifurcation analysis in Ref. [63]. In analogy to panel Fig. 2.6 (b), panel (a) shows the self-oscillation branch at delay $\tau = 500$ corresponding to the periodic orbit without feedback in Fig. 2.6. However, there are a number of other solutions, TLS_n, namely temporal localized states. Since the canard induces excitability in the region $v > 1$ close the AH bifurcation, we can generate TLSs by perturbing the system. It is numerically convenient to set the delay to the harmonics τ/n for $n \in \mathbb{N}$ because at sufficiently large delay, a train of n equidistant pulses has the same shape in our measure $\langle\cdot\rangle$ as a single pulse at delay τ/n. In panel (b), we see that period T of these TLSs is slightly longer than the delay τ, indicated by dotted lines, due to causality. The TLSs form a ladder-like structure that merges with the self-oscillation solution. This structure indicates that the self-oscillation is, in fact, the limit where the whole temporal domain is filled with pulses. As we shall see

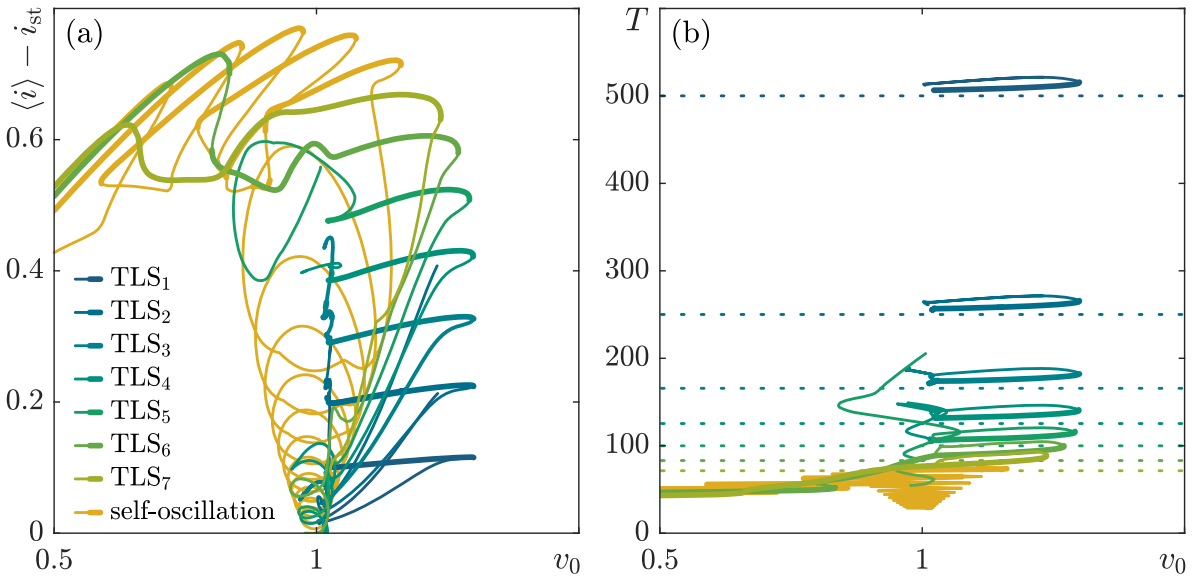

Figure 2.7: Bifurcation diagram in the bias voltage v_0 of the delayed FHN model with feedback strength $\kappa = 0.18$ and stiffness $\varepsilon = 0.05$. As measures on the ordinate, we chose with (a) the deviation of the average current from the steady state, $\langle i \rangle - i_{\mathrm{st}}$ and (b) the period T. The delay for the self-oscillation is $\tau = 500$. The dotted lines in panel (b) show the delay $\tau = 500/n$ for the respective TLS$_n$.

below, the findings presented here bear importance for understanding the more complicated RTD-LD.

3 Model system and methods

The RTD-LD is an optoelectronic circuit capable of self-oscillation, generating pulses from perturbations, and sustaining these pulses through time-delayed feedback. In Fig. 2.8 (a), we illustrate the basic operating principle: Here, the RTD oscillates in the voltage v and the current i, which drives the laser carrier number n. In turn, the carrier number interacts with the photon number s through spontaneous and stimulated emission. The resulting light pulse travels back to the RTD via an optical fiber, which induces a delay time τ. Such a pulse, as exemplified in panel (b), is a clockwise orbit in the phase space of the RTD in panel (c) as well as that of the laser in panel (d). Once the delayed light pulse reaches the RTD, it results in a photocurrent that affects the voltage v. This time-delayed feedback renders the RTD-LD an *autaptic* neuron [3, 25], akin to a chain of identical neurons, which allows us to

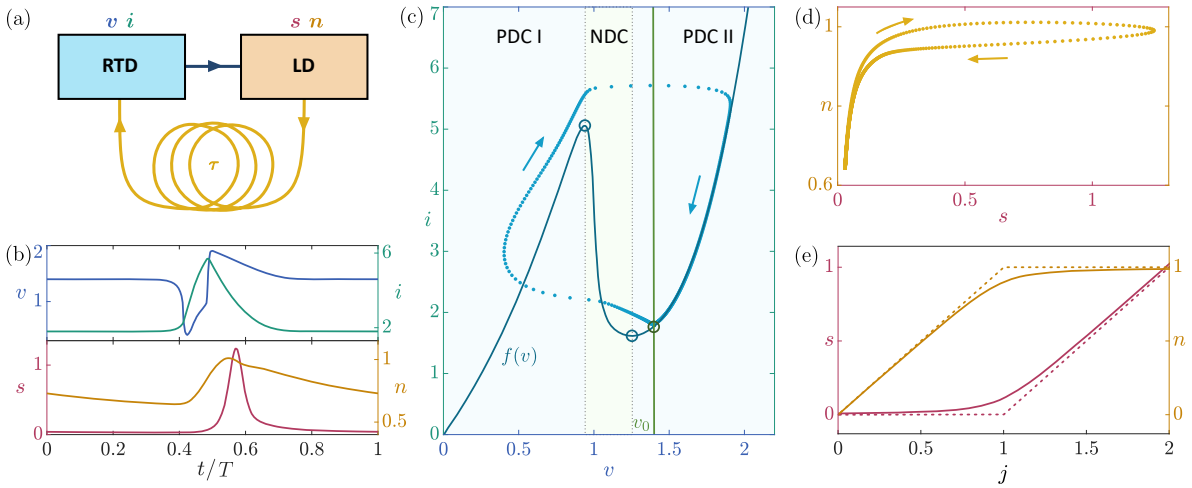

Figure 2.8: (a) Schematic of the RTD-LD with feedback of time delay τ. The dynamic variables are the voltage v and the current i for the RTD, as well as the photon number s and the carrier number n for the LD. (b) Time trace of an excited pulse at bias voltage $v_0 = 1.4$. (c) Phase space of the RTD: Nonlinear current-voltage characteristic $f(v)$ of the RTD-LD (dark blue line), local extrema of $f(v)$ (dark blue circles), load line $v_0 = v - ri$ (green line), and the resulting operating point (green circle), along with the excited pulse from (b) (light blue), PDC regions (blue regions), and NDC region (green region). (d) Phase space of the LD with the excited pulse from (b). (e) Equilibrium states of the LD depending on the bias current j for $\eta = 0$. The exact solution (solid line) approximates the transcritical bifurcation (dotted line) for $\gamma_m/\gamma_t \to 0$.

study information propagation and memory with much lower computational cost.

The model of the RTD-LD comprises a set of four DDEs in time t for the voltage $v(t)$, the current $i(t)$, the photon number $s(t)$, and the carrier number $n(t)$

$$t_\mathrm{v}\,\dot{v} = i - f(v) - \kappa s(t-\tau)\,, \tag{3.1}$$

$$t_\mathrm{i}\;\dot{i} = v_0 - v - ri\,, \tag{3.2}$$

$$t_\mathrm{s}\,\dot{s} = (n-1)s + \frac{\gamma_\mathrm{m}}{\gamma_\mathrm{t}}(n_0+n)\,, \tag{3.3}$$

$$t_\mathrm{n}\dot{n} = j + \eta i - n(1+s)\,. \tag{3.4}$$

The parameters are the current-voltage characteristic $f(v)$, the feedback strength κ from the LD to the RTD with delay τ, the bias voltage v_0, the resistance r, the spontaneous emission into the lasing mode γ_m and the total decay rate γ_t, the transparency carrier number n_0, the injection efficiency η of the RTD into the LD, and finally the bias current j. Each of the variables v, i, s, and n has its own characteristic time scale t_v, t_i, t_s, and t_n, respectively. This is evident from the time trace of a typical periodic solution of period T shown in Fig. 2.8 (b).

Note that the RTD is a slow-fast system based on resonant-tunneling through a double-quantum well [10]: While the voltage v changes quickly on the time scale t_v, the current i follows slowly on the time scale t_i, see Fig. 2.8 (b) and (c). From Eqs. (3.1) and (3.2), we can easily deduce that the steady state of the RTD lies at the intersection of the nullclines $i = f(v)$ and $i = (v_0 - v)/r$. Assuming a very small resistance r, the slope of the latter nullcline is nearly vertical, which guarantees that for every bias voltage v_0, there is only one intersection point with $f(v)$ at $v \approx v_0$, as shown in Fig. 2.8 (c). The stability of this fixed point, however, varies with the bias voltage v_0, which is another important parameter determining the RTD-LD dynamics.

Without feedback, i.e., for $\kappa = 0$, the RTD Eqs. (3.1) and (3.2) are equivalent to the classic FitzHugh–Nagumo (FHN) model [17, 54], except that the current-voltage characteristic $f(v)$

is not the cubic polynomial $-v + v^3/3$ but the function

$$\begin{aligned} f(v) = \operatorname{sign}(a) \log\left(\frac{1+\exp\left(\frac{q_\mathrm{e}}{k_\mathrm{B}T}(b-c+n_1 v)\right)}{1+\exp\left(\frac{q_\mathrm{e}}{k_\mathrm{B}T}(b-c-n_1 v)\right)}\right) \\ \left[\frac{\pi}{2} + \arctan\left(\frac{c-n_1 v}{d}\right)\right] \\ + \frac{h}{|a|}\left[\exp\left(\frac{q_\mathrm{e}}{k_\mathrm{B}T} n_2 v\right) - 1\right], \end{aligned} \tag{3.5}$$

where a, b, c, d, h, n_1, and n_2 are fit parameters, q_e is the elementary charge, k_B is the Boltzmann constant, and T is the temperature. This expression is derived in Ref. [67] by mixing first-principle calculations with a fit of experimental data of RTDs. The slope of $f(v)$ is the differential conductance and, for typical parameters (see Appendix A), the characteristic has a region of *negative* differential conductance (NDC) in between two regions of *positive* differential conductance (PDC I and PDC II), cf. Fig. 2.8 (c). The NDC region is the key property of RTDs and precisely in this region, the steady state loses stability, leading to self-oscillation, as we shall discuss in more detail in Section 4.1.

The LD, being a class-B laser, is a slow-fast system too, see Fig. 2.8 (b) and (d): The photon number s is fast on the time scale $t_\mathrm{s} = \tau_\mathrm{s}/t_\mathrm{c}$ with photon lifetime τ_s. Once excited by the current i with an efficiency η, the slow carrier number n returns to equilibrium with an exponential decay on the time scale $t_\mathrm{n} = \tau_\mathrm{n}/t_\mathrm{c}$, where $\tau_\mathrm{n} = 1/\gamma_\mathrm{t}$ is the carrier lifetime. Conversely, $\gamma_\mathrm{t} = \gamma_\mathrm{l} + \gamma_\mathrm{m} + \gamma_\mathrm{nr}$ is the total decay rate, consisting of the spontaneous emission in the leaky modes γ_l and the lasing mode γ_m, as well as the non-radiative recombination γ_nr. The ratio $\gamma_\mathrm{m}/\gamma_\mathrm{t} = \beta\mathrm{QE}$ is the product of the spontaneous coupling rate β [62] and the quantum efficiency QE (cf. Eqs. (3.36) and (3.37)). We choose the bias parameter $j \approx -0.43$ in the off-state near an approximate transcritical bifurcation at $j = 1$ (which is exactly a transcritical bifurcation for $\gamma_\mathrm{m}/\gamma_\mathrm{t} \to 0$) so that the laser turns on intermittently when driven by the RTD, see Fig. 2.8 (e).

In the following, we derive the RTD-LD model (3.1)-(3.4) on the basis of a model presented in Section 3.1 by performing a change of variables in Section 3.2 and a non-dimensionalization in Section 3.3. Finally, we introduce the slow-RTD approximation in Section 3.4 and present our numerical methods in Section 3.5.

3.1 Physical model

The physical model for the voltage V, current I, electric field E, and carrier number N, adapted from Ref. [57] by adding a time-delayed feedback from the laser to the RTD, reads

$$C\dot{V} = I - f(V) - \kappa|E(t-\tau)|^2 + \sigma\xi_{\mathrm{V}}(t)\,, \tag{3.6}$$

$$L\dot{I} = V_0(t) - V - RI\,, \tag{3.7}$$

$$\dot{E} = \frac{1-\mathrm{i}\alpha}{2}\left[G - \frac{1}{\tau_{\mathrm{s}}}\right]E + \sqrt{\frac{\gamma_{\mathrm{m}}N}{2}}[\xi_{\mathrm{x}}(t) + \mathrm{i}\xi_{\mathrm{y}}(t)]\,, \tag{3.8}$$

$$\dot{N} = \frac{J+\eta I}{q} - \gamma_{\mathrm{t}}N - G|E|^2 \tag{3.9}$$

with the total decay rate $\gamma_{\mathrm{t}} = \gamma_{\mathrm{l}} + \gamma_{\mathrm{m}} + \gamma_{\mathrm{nr}}$, gain $G = \gamma_{\mathrm{m}}(N - N_0)$, and the parameters listed in Appendix A. The photon number S is related to the complex electrical field $E = E_{\mathrm{x}} + \mathrm{i}E_{\mathrm{y}}$ via $S = |E|^2 = E_{\mathrm{x}}^2 + E_{\mathrm{y}}^2$. As our model shall just consider the field intensity S, we set the Henry factor $\alpha = 0$ without loss of generality. Note that Eqs. (3.6)-(3.9) are stochastic delay-differential equations with uncorrelated Gaussian white noise ξ_{V}, ξ_{x}, and ξ_{y} with zero mean $\mathbb{E}[\xi] = 0$ and auto-correlation $\langle\xi(t_1)\xi(t_2)\rangle = \delta(t_1 - t_2)$. For the scope of our analysis, however, we shall assume the noise in the RTD to be negligible by setting $\sigma = 0$, in accordance with time simulations.

3.2 Change of variables

To arrive at a deterministic model, we aim to average the noise from the stochastic processes ξ_{x} and ξ_{y}. It turns out to be convenient to use the photon number S rather than the complex electric field E. For the transformation from E to S, consider an *Itô drift-diffusion process* that satisfies the stochastic differential equation $\mathrm{d}\vec{E}(t) = \vec{A}\mathrm{d}t + \mathbf{B}\mathrm{d}\vec{w}$, where we write the complex field as a vector $\vec{E} = (E_{\mathrm{x}}, E_{\mathrm{y}})^{\mathrm{T}}$ of real and imaginary parts, with $\vec{A} = \frac{1}{2}a\vec{E}$ and $\mathbf{B} = b\,\mathrm{id}$, and the

Wiener process (*Brownian motion*) $\mathrm{d}\vec{w} = (\xi_\mathrm{x}(t+\mathrm{d}t) - \xi_\mathrm{x}(t), \xi_\mathrm{y}(t+\mathrm{d}t) - \xi_\mathrm{y}(t))^\mathrm{T}$. In our model,

$$a = G - \frac{1}{\tau_\mathrm{s}}, \tag{3.10}$$

$$b = \sqrt{\gamma_\mathrm{m} N/2}\,. \tag{3.11}$$

Itô's formula states that for any transformation $g(t,x)$ (which is C^2) of an n-dimensional Itô process $\mathrm{d}\vec{X}(t) = \vec{A}\mathrm{d}t + \mathbf{B}\mathrm{d}\vec{w}$, the kth component of the Itô process $\vec{Y}(t) = \vec{g}(t, \vec{X}(t))$ is described by [55, pp. 48]

$$\mathrm{d}Y_k = \frac{\partial g_k}{\partial t}\mathrm{d}t + \sum_{i=1}^{n} \frac{\partial g_k}{\partial x_i}\mathrm{d}X_i + \frac{1}{2}\sum_{i,j=1}^{n} \frac{\partial g_k}{\partial x_i \partial x_j}\mathrm{d}X_i \mathrm{d}X_j\,. \tag{3.12}$$

Consequently, for $g(t,x) = |\vec{x}|^2$ and $S(t) = g(t, \vec{E}(t))$, we arrive after some calculation (using that $\mathrm{d}X_i\mathrm{d}X_j = \sum_{k=1}^{n} B_{ik}B_{jk}\mathrm{d}t$ in this expansion to order $\mathrm{d}t$ because $\mathrm{d}w_i = O(\sqrt{\mathrm{d}t})$ and $\mathrm{d}w_i\mathrm{d}w_j = \delta_{ij}\mathrm{d}t$) at

$$\begin{aligned} \mathrm{d}S &= \sum_{i=1}^{n} \frac{\partial g}{\partial x_i}\mathrm{d}X_i + \frac{1}{2}\sum_{i,j=1}^{n} \frac{\partial^2 g}{\partial x_i \partial x_j}\mathrm{d}X_i\mathrm{d}X_j \\ &= aS\mathrm{d}t + 2b^2\mathrm{d}t + 2b(E_\mathrm{x}\mathrm{d}w_\mathrm{x} + E_\mathrm{y}\mathrm{d}w_\mathrm{y})\,. \end{aligned} \tag{3.13}$$

Introducing the phase $\phi = \mathrm{atan2}(E_\mathrm{y}, E_\mathrm{x})$ of the field $\vec{E}$, we write the last term as

$$2b\left(\sqrt{S}\cos(\phi)\mathrm{d}w_\mathrm{x} + \sqrt{S}\sin(\phi)\mathrm{d}w_\mathrm{y}\right), \tag{3.14}$$

which is well defined since the noise variance goes to zero once S approaches zero. So we can define a new stochastic process

$$\mathrm{d}w_\mathrm{S} = \left(\cos(\phi)\mathrm{d}w_\mathrm{x} + \sin(\phi)\mathrm{d}w_\mathrm{y}\right), \tag{3.15}$$

where ξ_S defined by $\mathrm{d}w_\mathrm{S} = \xi_\mathrm{S}(t+\mathrm{d}t) - \xi_\mathrm{S}(t)$ is again a Wiener process since $\mathbb{V}[\xi_\mathrm{S}] = \cos^2(\phi)\mathbb{V}[\xi_\mathrm{x}] + \sin^2(\phi)\mathbb{V}[\xi_\mathrm{y}] = 1$. With these definitions, we have

$$\mathrm{d}S = (aS + 2b^2)\mathrm{d}t + 2b\sqrt{S}\mathrm{d}w_\mathrm{S}\,, \tag{3.16}$$

and reinserting a and b from above,

$$\dot{S} = \left(G - \frac{1}{\tau_s}\right)S + \gamma_m N + \sqrt{2\gamma_m N S}\xi_S(t)\,, \tag{3.17}$$

with noise variance $2\gamma_m NS$. Note that Ref. [57] is missing a factor 2 in the variance.

3.3 Non-dimensionalization

We define the dimensionless time $\tilde{t}$ and delay $\tilde{\tau}$ through $t = t_c\tilde{t}$ and $\tau = t_c\tilde{\tau}$, respectively, with the characteristic time scale t_c. Similarly, $V = v_c v$, $V_0 = v_c v_0$, $I = i_c i$, $S = s_c s$, and $N = n_c n + N_0$ define the dimensionless system variables (v, i, s, n) and the bias voltage v_0. We shall determine a natural selection of characteristic scales by calculating the steady states of the system or approximations thereof.

First, let us consider the steady state of the RTD. We see from Eq. (3.6) that the fixed points without feedback ($\kappa = 0$) are determined by $I = f(V)$ and $V \approx V_0$ if the resistance R is small. The current-voltage characteristic $f(V)$ has a jump height of order a around $c - n_1 V = 0$, i.e., at $V = c/n_1$. With the characteristic scale for voltage and current defined as $v_c = c/n_1$ and $i_c = |a|$, the new function $\tilde{f}(v) = f(V/v_c)/i_c$ has a jump of order 1 around $v = 1$.

Next, we shall find the steady states of the LD. Solving $\dot{S} = 0$ and $\dot{N} = 0$ with Eqs. (3.17) and (3.9) in the limit of a large laser (where $\gamma_m/\gamma_t = 0$), ignoring the average noise $\gamma_m N$, and assuming the current injection I to be constant here for simplicity, we get two solutions: the off-state

$$N_{off} \approx \frac{J + \eta I}{\gamma_t q}\,, \tag{3.18}$$

$$S_{off} \approx 0\,, \tag{3.19}$$

in which the laser does not emit photons, and the on-state

$$N_{on} \approx n_c(1 + n_0)\,, \tag{3.20}$$

$$S_{on} \approx \frac{\tau_s j_c}{q}\left(j + \tilde{\eta} i - 1\right), \tag{3.21}$$

where $n_c = 1/(\tau_s\gamma_m)$ is the characteristic scale along with the dimensionless transparency

carrier number defined by $N_0 = n_c n_0$. We set the characteristic bias current to $j_c = q\gamma_t n_c = \frac{q\gamma_t}{\tau_s\gamma_m}$ such that $J = j_c(j + n_0)$ and let $\tilde{\eta} = \eta i_c/j_c$. A natural choice for the characteristic photon number is

$$s_c = \frac{\tau_s j_c}{q} = \frac{\gamma_t}{\gamma_m} = \frac{1}{\tau_n\gamma_m}\,. \tag{3.22}$$

In summary, the characteristic scales of the system variables and parameters are

$$v_c = c/n_1\,, \tag{3.23}$$
$$i_c = |a|\,, \tag{3.24}$$
$$s_c = 1/(\tau_n\gamma_m)\,, \tag{3.25}$$
$$n_c = 1/(\tau_s\gamma_m)\,, \tag{3.26}$$
$$j_c = q\gamma_t n_c\,, \tag{3.27}$$
$$\kappa_c = i_c/s_c\,, \tag{3.28}$$
$$r_c = v_c/i_c\,, \tag{3.29}$$
$$\eta_c = j_c/i_c\,, \tag{3.30}$$

where we also define the dimensionless resistance $r = R/r_c$ and feedback strength $\tilde{\kappa} = \kappa/\kappa_c$.

To complete the derivation, we determine a characteristic time scale for the RTD and each of the four system variables (v, i, s, n). We begin by inserting the definitions (3.23) to (3.30) of the rescaled variables into the system equations (3.6), (3.7), (3.17), and (3.9),

$$\frac{Cv_c}{i_c t_c}\frac{\mathrm{d}v}{\mathrm{d}\tilde{t}} = i - \tilde{f}(v) - \tilde{\kappa}s(\tilde{t} - \tilde{\tau})\,, \tag{3.31}$$
$$\frac{Li_c}{v_c t_c}\frac{\mathrm{d}i}{\mathrm{d}\tilde{t}} = v_0 - v - ri\,, \tag{3.32}$$
$$\frac{\tau_s}{t_c}\frac{\mathrm{d}s}{\mathrm{d}\tilde{t}} = (n-1)s + \frac{\gamma_m}{\gamma_t}(n + n_0) + \sqrt{2\tau_s\tau_n\gamma_m(n + n_0)s}\,\xi_S(t)\,, \tag{3.33}$$
$$\frac{\tau_n}{t_c}\frac{\mathrm{d}n}{\mathrm{d}\tilde{t}} = j + \tilde{\eta}i - n(1 + s)\,. \tag{3.34}$$

Although noise can have a profound impact on the dynamics of a system [37], the noise here appears to be negligible *after* the change of variables because, for typical parameters, the value $\sqrt{2\tau_s\tau_n\gamma_m} \approx 6\cdot 10^{-8}$ is much smaller than n and s, which are of order one. Furthermore, time simulations verify that neglecting the noise is justified. Alternatively, we could derive the Fokker-Planck equation to obtain differential equations for the expected value of the state vector (v, i, s, n), but this would complicate matters unnecessarily. Notably, the prefactor of

the average noise is

$$\frac{\gamma_{\mathrm{m}}}{\gamma_{\mathrm{t}}} = \beta \mathrm{QE}\,, \tag{3.35}$$

where the *spontaneous emission coupling factor* [62],

$$\beta = \frac{\gamma_{\mathrm{m}}}{\gamma_{\mathrm{r}}}\,, \tag{3.36}$$

is nonzero if the laser is small and the quantum efficiency is defined as

$$\mathrm{QE} = \frac{\gamma_{\mathrm{r}}}{\gamma_{\mathrm{r}} + \gamma_{\mathrm{nr}}} \tag{3.37}$$

with the radiative decay rate $\gamma_{\mathrm{r}} = \gamma_{\mathrm{m}} + \gamma_{\mathrm{l}}$ and the total decay rate $\gamma_{\mathrm{t}} = \gamma_{\mathrm{r}} + \gamma_{\mathrm{nr}}$.

By setting

$$\mu = \frac{C v_{\mathrm{c}}}{i_{\mathrm{c}} t_{\mathrm{c}}} = \left(\frac{L i_{\mathrm{c}}}{v_{\mathrm{c}} t_{\mathrm{c}}}\right)^{-1}, \tag{3.38}$$

and solving the condition

$$1 = \mu\mu^{-1} = \frac{LC}{t_{\mathrm{c}}^2} \tag{3.39}$$

for the characteristic time scale t_{c} of the RTD, we obtain

$$t_{\mathrm{c}} = \sqrt{LC}\,. \tag{3.40}$$

A natural time scale of the photon number is the photon lifetime τ_{s}, while for the carrier number the time scale is the carrier lifetime τ_{n}. Since only the relative time scale of the LD versus the RTD is important for the dynamics of the system, we define the characteristic time scales of the LD relative to t_{c}, i.e.,

$$t_{\mathrm{v}} = \mu\,, \tag{3.41}$$

$$t_{\mathrm{i}} = \mu^{-1}\,, \tag{3.42}$$

$$t_{\mathrm{s}} = \tau_{\mathrm{s}}/t_{\mathrm{c}}\,, \tag{3.43}$$

$$t_{\mathrm{n}} = \tau_{\mathrm{n}}/t_{\mathrm{c}}\,. \tag{3.44}$$

We thus arrive at the system equations

$$t_{\mathrm{v}}\frac{\mathrm{d}v}{\mathrm{d}\tilde{t}} = i - \tilde{f}(v) - \tilde{\kappa}s(\tilde{t}-\tilde{\tau})\,, \tag{3.45}$$

$$t_{\mathrm{i}}\frac{\mathrm{d}i}{\mathrm{d}\tilde{t}} = v_0 - v - ri\,, \tag{3.46}$$

$$t_{\mathrm{s}}\frac{\mathrm{d}s}{\mathrm{d}\tilde{t}} = (n-1)s + \frac{\gamma_{\mathrm{m}}}{\gamma_{\mathrm{t}}}(n+n_0)\,, \tag{3.47}$$

$$t_{\mathrm{n}}\frac{\mathrm{d}n}{\mathrm{d}\tilde{t}} = j + \tilde{\eta}i - n(1+s)\,. \tag{3.48}$$

Outside of this section, we omit the tilde on $\tilde{f}$, $\tilde{t}$, $\tilde{\tau}$, and $\tilde{\eta}$ and take the dot to mean the derivative with respect to $\tilde{t}$, e.g., $\dot{v} = \mathrm{d}v/\mathrm{d}\tilde{t}$.

3.4 Slow-RTD approximation

Our analysis of the RTD-LD system (3.1)-(3.4) focuses on the impact of the laser nonlinearity and the RTD time scale on the behavior of TLSs. When the RTD is very slow (i.e., $\min(t_{\mathrm{v}}, t_{\mathrm{i}}) \gg \max(t_{\mathrm{s}}, t_{\mathrm{n}})$), the laser equilibrates almost instantly relative to the characteristic time scale of the RTD. In this case, we can adiabatically reduce the four-dimensional system state (v, i, s, n) to the two-dimensional state (v, i) by setting $\dot{s} = 0$ and $\dot{n} = 0$. With Eqs. (3.3) and (3.4), this leads to

$$0 = (n-1)s + \frac{\gamma_{\mathrm{m}}}{\gamma_{\mathrm{t}}}(n_0+n)\,, \tag{3.49}$$

$$0 = \hat{j} - n(1+s)\,, \tag{3.50}$$

where we define the combined bias current $\hat{j}(t) = j + \eta i(t)$ for brevity. Solving this system of equations, we arrive at an approximation of the delayed term $s(t-\tau)$ by the nonlinear function

$$s(t) = \frac{1}{2}\Bigg(v - 1 + \hat{j} + \sqrt{(1+v)^2 + 2\left(\frac{\gamma_{\mathrm{m}}}{\gamma_{\mathrm{t}}}(n_0+2) - 1\right)\hat{j} + \hat{j}^2}\Bigg) \tag{3.51}$$

with the shorthand $\nu = \frac{\gamma_m}{\gamma_t} n_0$. The system equations are thus

$$t_v \dot{v} = i - f(v) - \kappa s(t - \tau)\,, \tag{3.52}$$

$$t_i \dot{i} = v_0 - v - ri\,. \tag{3.53}$$

Importantly, the simplified system, Eqs. (3.52) and (3.53), is closely related to the prototypical delayed FitzHugh–Nagumo model of the RTD in Ref. [63] expect for the more realistic current-voltage characteristic $f(v)$ and the non-Pyragas feedback term [60, 66].

3.5 Numerical methods

In the theoretical analysis of the RTD-LD system, we employ both time simulations and path-continuation methods. The path-continuation for the bifurcation analysis of the DDE system (3.1)-(3.4) relies on the MATLAB package DDE-BIFTOOL [14]. The code for the bifurcation analysis and corresponding visualizations of the bifurcation diagrams are freely available [47].

The specific parameter values we fixed in the following for concreteness of the model are listed in Appendix A. Unless mentioned otherwise, the delay time is fixed at $\tau = 20$. Furthermore, we classify the characteristic time scale, defined as the RTD self-oscillation (tank) frequency $t_c = \sqrt{LC}$ in Eq. (3.40), into two regimes. For the fast RTD, we select $t_{c,\mathrm{fast}} \approx 15.9\,\mathrm{ps}$ with capacitance $C = 2\,\mathrm{fF}$ and inductance $L = 126\,\mathrm{nH}$. In contrast, for the slow RTD, we set $t_{c,\mathrm{slow}} \approx 15.9\,\mathrm{ns}$ with $C = 2\,\mathrm{pF}$ and inductance $L = 126\,\mu\mathrm{H}$. The slow RTD thus operates a thousand times slower than the fast RTD so that the slow-RTD approximation applies.

To solve the RTD-LD system (3.1)-(3.4) through time simulation, we use a semi-implicit method. The coupling between the RTD and the LD is directed in the sense that the LD does not influence the RTD instantly, which means that within each step, we can first solve the RTD and then the LD. While we choose time steps $t_k = kh$ with step size h and $k \in \mathbb{N}$ for the variables (i, v, s), the carrier number n is calculated as split-stepping at $t_{k+\frac{1}{2}} = (k + \frac{1}{2})h$.

We obtain the numerical scheme by integrating the system equations (3.1)-(3.4) over one time step and averaging the variables between time steps. For the RTD, the discretization

leads to

$$t_{\mathrm{v}}(v_{k+1} - v_k) = \frac{h}{2}(i_k + i_{k+1}) - \int_{t_k}^{t_{k+1}} \mathrm{d}t\, f(v) - \frac{h}{2}\kappa(s_{k-\bar{\tau}} + s_{k+1-\bar{\tau}})\,, \tag{3.54}$$

$$t_{\mathrm{i}}(i_{k+1} - i_k) = hv_0 - \frac{h}{2}(v_k + v_{k+1}) - \frac{h}{2}r(i_k + i_{k+1})\,, \tag{3.55}$$

where the number of delay time steps is $\bar{\tau} = \lceil \tau/h \rceil$ defined by the ceiling value (the smallest integer larger than τ/h).

To approximate the integral, a Taylor expansion of $v(t)$ around t_k to first order in t and subsequently of $f(v)$ around v_k to first order in h,

$$\begin{aligned}\int_{t_k}^{t_{k+1}} \mathrm{d}t\, f(v) &= \int_{t_k}^{t_{k+1}} \mathrm{d}t\, f\left(v_k + \frac{t}{h}(v_{k+1} - v_k) + O(t^2)\right) \\ &= \int_{t_k}^{t_{k+1}} \mathrm{d}t \left[f(v_k) + \frac{t + O(t^2)}{h}(v_{k+1} - v_k) f'(v_k)\right] \\ &= hf(v_k) + \frac{h}{2}(v_{k+1} - v_k) f'(v_k) + O(h^2)\,,\end{aligned} \tag{3.56}$$

yields

$$t_{\mathrm{v}}(v_{k+1} - v_k) = \frac{h}{2}(i_k + i_{k+1}) - hf(v_k) - \frac{h}{2}(v_{k+1} - v_k) f'(v_k) - \frac{h}{2}\kappa(s_{k-\bar{\tau}} + s_{k+1-\bar{\tau}})\,, \tag{3.57}$$

$$t_{\mathrm{i}}(i_{k+1} - i_k) = hv_0 - \frac{h}{2}(v_k + v_{k+1}) - \frac{h}{2}r(i_k + i_{k+1})\,. \tag{3.58}$$

Collecting the terms of step $k+1$ on the left, we rewrite the equations as

$$a_{11}v_{k+1} + a_{12}i_{k+1} = b_1\,, \tag{3.59}$$

$$a_{21}v_{k+1} + a_{22}i_{k+1} = b_2\,, \tag{3.60}$$

so that the solution for the step $k+1$ of RTD is

$$v_{k+1} = \frac{a_{22}b_1 - a_{12}b_2}{a_{11}a_{22} - a_{12}a_{21}}, \tag{3.61}$$

$$i_{k+1} = \frac{a_{11}b_2 - a_{21}b_1}{a_{11}a_{22} - a_{12}a_{21}}, \tag{3.62}$$

with

$$\begin{pmatrix} a_{11} & a_{12} \\ a_{21} & a_{22} \end{pmatrix} = \begin{pmatrix} t_\mathrm{v} + \frac{h}{2}f'(V_k) & -\frac{h}{2} \\ \frac{h}{2} & t_\mathrm{i} + \frac{h}{2}r \end{pmatrix} \tag{3.63}$$

and

$$\begin{pmatrix} b_1 \\ b_2 \end{pmatrix} = \begin{pmatrix} \frac{h}{2}i_k + t_\mathrm{v}v_k - h\left[f(v_k) - \frac{v_k}{2}f'(v_k)\right] \\ hv_0 - \frac{h}{2}(v_k + ri_k) + t_\mathrm{i}i_k \end{pmatrix}. \tag{3.64}$$

The derivative $f'(v)$ necessary for the calculation is

$$\begin{aligned} f'(v) = &- \operatorname{sign}(a) n_1 \frac{\log\left(\frac{F^+(v)+1}{F^-(v)+1}\right)}{d\left(\frac{(c-n_1 v_\mathrm{c} v)^2}{d^2} + 1\right)} \\ &- \operatorname{sign}(a) n_1 \frac{q}{k_\mathrm{B}T} \frac{F^+(v) + F^-(v)\frac{F^+(v)+1}{F^-(v)+1}}{F^+(v)+1} \\ &\arctan\left(\frac{c - n_1 v_\mathrm{c} v}{d} + \frac{\pi}{2}\right) \\ &+ \frac{h}{|a|} n_2 \frac{q}{k_\mathrm{B}T} \mathrm{e}^{\frac{q}{k_\mathrm{B}T} n_2 v_\mathrm{c} v} \end{aligned} \tag{3.65}$$

with the abbreviation

$$F^\pm(v) = \mathrm{e}^{\frac{q}{k_\mathrm{B}T}(b - c \pm n_1 v_\mathrm{c} v)}. \tag{3.66}$$

For the LD, we arrive at

$$\begin{aligned} t_\mathrm{s}\left(s_{k+1} - s_k\right) = &\frac{h}{2}\left(n_{k+\frac{1}{2}} - 1\right)\left(s_{k+1} + s_k\right) \\ &+ h\frac{\gamma_\mathrm{m}}{\gamma_\mathrm{t}}\left(n_{n+\frac{1}{2}} + n_0\right) \\ &+ \sqrt{2h\tau_\mathrm{s}\tau_\mathrm{n}\gamma_\mathrm{m}(n_{k+\frac{1}{2}} + n_0)s_k}\,\xi_{\mathrm{S},k}(t), \end{aligned} \tag{3.67}$$

where s_k in the optional noise term approximates $(s_{k+1} + s_k)/2$, and by solving for s_{k+1}, we

get

$$s_{k+1} = \frac{\left(t_\mathrm{s} + \frac{h}{2}\left(n_{k+\frac{h}{2}} - 1\right)\right)s_k + h\frac{\gamma_\mathrm{m}}{\gamma_\mathrm{t}}\left(n_{n+\frac{1}{2}} + n_0\right)}{t_\mathrm{s} - \frac{h}{2}\left(n_{k+\frac{h}{2}} - 1\right)}. \tag{3.68}$$

Similarly, we derive from

$$\begin{aligned} t_\mathrm{n}\left(n_{k+\frac{3}{2}} - n_{k+\frac{1}{2}}\right) = h(\eta i_{k+1} + j) \\ - \frac{h}{2}\left(n_{k+\frac{1}{2}} + n_{k+\frac{3}{2}}\right)(1 + s_{k+1}) \end{aligned} \tag{3.69}$$

that

$$n_{k+\frac{3}{2}} = \frac{\left(t_\mathrm{n} - \frac{h}{2}(1 + s_{k+1})\right)n_{k+\frac{1}{2}} + h(\eta i_{k+1} + j)}{t_\mathrm{n} + \frac{h}{2}\left(1 + s_{k+1}\right)}. \tag{3.70}$$

In summary, Eqs. (3.61), (3.62), (3.68), and (3.70) define the scheme for a time simulation of the RTD-LD model.

4 Results and discussion

4.1 No feedback

To understand the influence of the delayed feedback on the system in question, let us first review how the RTD system (3.1)-(3.2) operates without feedback by setting $\kappa = 0$. A comprehensive bifurcation analysis of this case has been performed in Ref. [56]. The bifurcation diagram in Fig. 4.1 shows that the steady state (black) indeed resembles $f(v)$ closely. On either side of the NDC region, the steady state loses its stability in a subcritical Andronov-Hopf (AH) bifurcation (white circles), so that the emerging periodic solution (green) coexists with the steady state in a small region of bistability within PDC II. The sudden increase in the amplitude of the limit cycle around the bifurcation points a *canard explosion* just like for the delayed FHN model in Section 2.3.

Given that the periodic solution does not rely on external perturbations and maintains a characteristic period T (cf. the inset in Fig. 4.1) that is largely independent of the delay τ, this

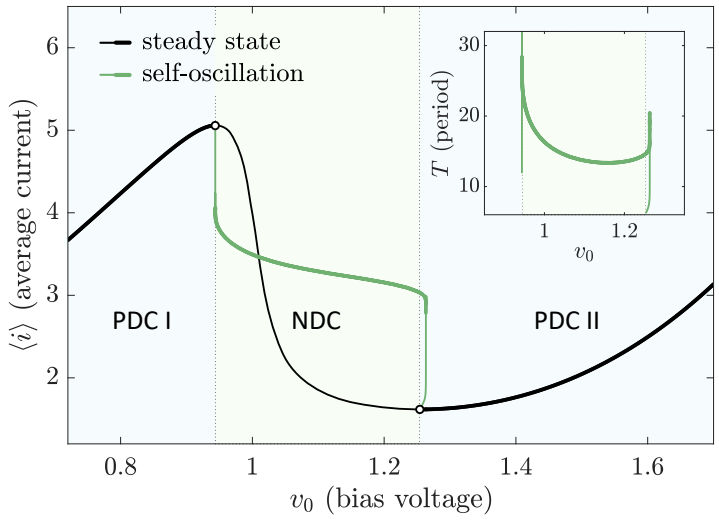

Figure 4.1: Bifurcation diagram of the RTD system (3.1)-(3.2) in the bias voltage v_0 without feedback ($\kappa = 0$). The thick lines represent stable solutions, the thin lines unstable solutions. The self-oscillation branch (green) attaches to the steady state (black) through two subcritical Andronov-Hopf bifurcations (white circles). In the inset, the period T of the self-oscillation branch is shown.

solution is called *self-oscillation*. Figure 4.1 shall serve as reference point for our subsequent analysis to comprehend how time-delayed feedback alters this picture.

4.2 Regime of the slow RTD

Let us now turn to the effect of time-delayed feedback on the RTD-LD dynamics in the slow-RTD approximation described in Section 3.4 by setting the characteristic time scale to $t_{\mathrm{c,slow}}$. Interestingly, a continuation of the corresponding DDE system (3.52)-(3.53) in the feedback strength κ for different values of v_0 as shown in Fig. 4.2 reveals that a new kind of solution emerges, see the inset for a typical time trace. This solution exists for a range of bias voltages v_0 in the PDC II region if the feedback is sufficiently strong. Note that the stable parts of all four branches diverge to infinity at $\kappa \approx 1.5$. The reason for this divergence is a feedback catastrophe, similar to that of a microphone held too close to a coupled loudspeaker: If the feedback is strong enough, each round trip in the circuit injects more and more energy into the circuit, which is proportional to the integral of the absolute value of the current, $\langle |i| \rangle$ (or simply $\langle i \rangle$ if i is positive).

To understand this new solution, we now fix the feedback strength at $\kappa = 1$ and follow

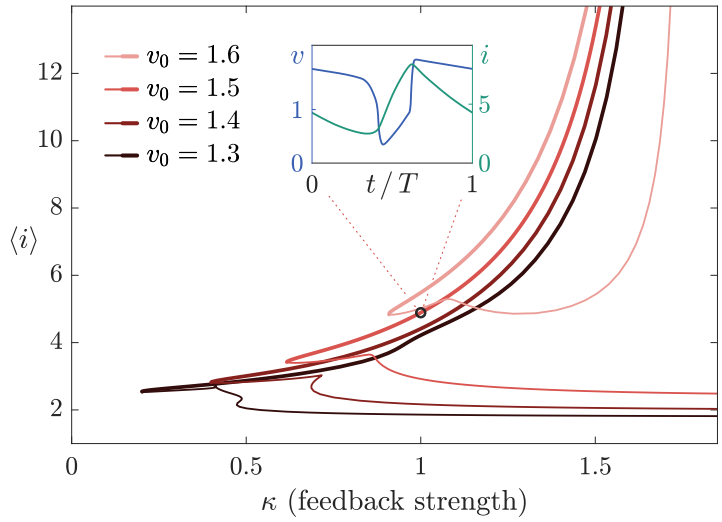

Figure 4.2: Bifurcation diagram of the the slow-RTD regime as given by Eqs. (3.52)-(3.53) in the feedback strength κ for four different values of v_0. The inset shows a typical solution profile.

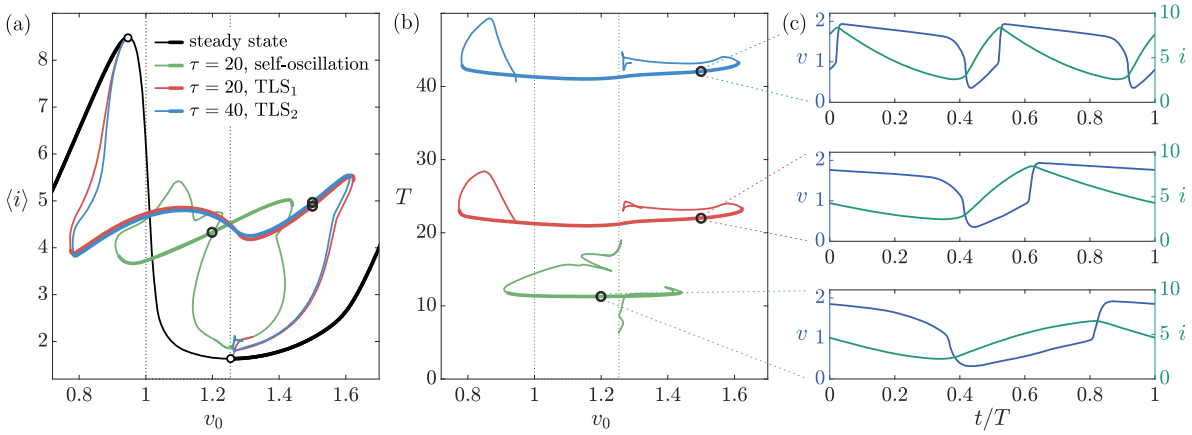

Figure 4.3: (a) Continuation in the bias voltage v_0 at $\kappa = 1$ in the slow-RTD regime. The steady state (black) loses its stability through two Andronov-Hopf bifurcations (white circles). (b) Period T of the corresponding periodic branches. (c) Time traces at $v_0 = 1.2$ for self-oscillation (green) and $v_0 = 1.5$ for the TLS$_1$ (red) and TLS$_2$ (blue). The position of the time traces in (a) and (b) is indicated by black circles. Vertical dashed lines separate the differential conductance regions.

the solutions of system (3.52)-(3.53) in the bias voltage v_0, see Fig. 4.3 (a). First, we observe that the steady state branch (black) has shifted relative to the case $\kappa = 0$ (cf. Fig. 4.1) because the non-Pyragas feedback term, $\kappa s(t-\tau)$, injects energy and thus raises the steady state to a higher average current $\langle i \rangle$, in contrast to the non-invasive Pyragas feedback, $\kappa\big(s(t-\tau)-s(t)\big)$, used in Ref. [63]. Second, the self-oscillation branch (green) has twisted into a loop and extends from the NDC into the PDC II region, separated by dashed vertical lines. However, the interesting difference to the case $\kappa = 0$ is a new solution type presented in Fig. 4.2: the red and the blue branch, labeled TLS_1 and TLS_2, which are one- and two-pulse *temporal localized states* (TLSs), respectively. They emerge from the steady state in an AH bifurcation and remain stable within the NDC and parts of the PDC I and II regions, see panel (c) for typical profiles. Note that we chose the measure in the bifurcation diagram such that the two branches TLS_1 at $\tau = 20$ and TLS_2 at $\tau = 40$ have a similar shape. A two-pulse state TLS_2 also exists for $\tau = 20$, just as the one-pulse state TLS_1 exists for $\tau = 40$. For any delay τ, there coexist as many TLS_n solutions as pulses can fit into the temporal domain. In fact, self-oscillation is the limit of the TLS_n where the entire domain is filled with tightly packed single-pulse TLSs, cf. Ref. [63]. We chose to double τ for TLS_2 because $\tau = 20$ would be too small to fit two pulses, but rendering TLS_1 would tax the computational efficiency. The fact that TLS_1 and TLS_2 connect to the left AH bifurcation at the boundary of the PDC I region is actually a finite-size effect of the relatively small temporal domains $\tau = 20$ and $\tau = 40$, which fit one and two pulses, respectively.

The nature of the TLSs becomes clearer when considering the period T in Fig. 4.3 (b) and corresponding time traces of one period at exemplary bias voltages (black circles) in panel (c). The stable part of the self-oscillation solution has a period of $T \approx 11$ and fills the entire domain with oscillations, as seen in the bottom plot of panel (c). In contrast, the period of the TLS_1, which is stable around $T \approx 22$, depends on the delay. In fact, its period $T = \tau + \delta$, is slightly larger by a drift δ than the delay τ due to causality [81]. Similarly, TLS_2 has double the period, $T = 2\tau + \delta_2 \approx 42$, with some other drift δ_2, as we can see from panel (b), cf. Ref. [82].

Let us emphasize that there are two significant features of the TLSs presented in Fig. 4.3 with respect to memory. First, the TLSs are bistable with the steady state. In conjunction with the excitability of the RTD, this bistability means that the stable steady state can be perturbed in the PDC II region, triggering a pulse. The TLSs are stabilized by the feedback, without

which the pulse would be a single excursion through the phase space and back to the steady state. However, the feedback is strong enough to sustain the pulse on its next round trip, emulating a series of neurons propagating the pulse.

Second, the TLS_2 solution in which the two TLSs are equidistant is stable. To explain this stability, the question is how two pulses racing around the RTD-LD circuit affect each other. An extremely useful method for answering this question is the *two-time representation* [1, 22, 81], often misleadingly referred to as *spatio-temporal* [1, 7, 42] or *space-time* representation [71] in an effort to highlight the deep connections between time-delayed and spatially extended systems [22]. The motivation for the two-time representation is to display dynamics on vastly different time scales, the period $T = \tau + \delta$ on the one hand and the dynamics over many round trips of the pulses within the circuit on the other. This representation is achieved by parameterizing time as $t = (\theta + \sigma)T$ via the number of round trips $\theta = \lfloor t/T \rfloor$ and the local time $\sigma = t/T \mod \theta$ within the most recent round trip, and then plotting the time trace in the (θ, σ)-plane. The current i of the time trace is best suited to represent the pulse dynamics, as it is a slow variable. Fig. 4.4 presents a two-time representation of a time simulation, initialized with two non-equidistant pulses (initial distance $d_0 = 0.17\tau$) within the temporal domain $[-\tau, 0)$. Note that if the pulses are initiated even closer to each other, time simulations show that both pulses die immediately and the system jumps to the steady state.

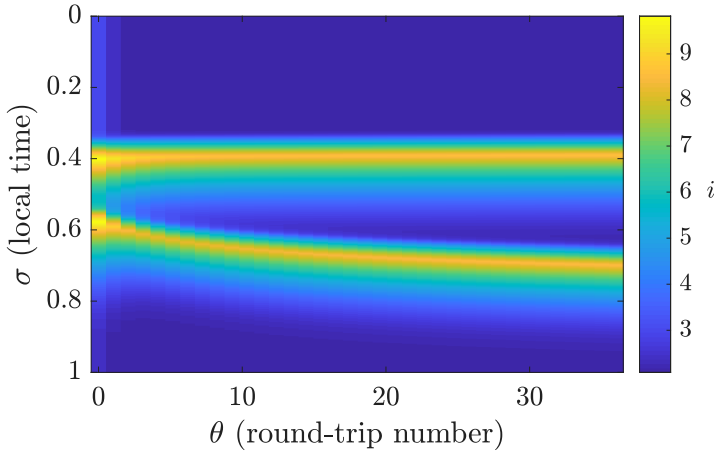

Figure 4.4: Two-time diagram of a TLS_2 in the slow-RTD regime. The pulses repel each other from an initial distance $d_0 = 0.17\tau \approx 0.166T$ in local time σ with feedback strength $\kappa = 1$ and delay $\tau = 80$ at bias voltage $v_0 = 1.5$. The local time σ is relative to the period $T = \tau + \delta \approx 81.8$ with the drift δ.

The key observation here is that, while a single pulse would move horizontally in the two-time diagram (since the drift δ has been accounted for in the definition of σ and θ), the two pulses *repel* each other. The non-reciprocal repulsive interaction is most pronounced for the second pulse starting at about $\sigma = 0.6$, but since the two-time parameterization transforms the time t into helical boundary conditions, the second pulse also interacts with the first.

It is well known that TLSs interact via tail overlap [77, 73], and in our case, as we operate in the slow-RTD regime, the dynamics are essentially controlled by the current i, which is the slowest variable. An interaction law between TLSs could be derived following, e.g., Ref. [51]. However, intuition about the excitability mechanism is sufficient to understand the nature of the repulsive forces. When the feedback arrives at the RTD to trigger the second TLS, the system has not quite reached the steady state yet since the trace of the first TLS is not completely lost. In particular, the value of the current i has not fully recovered. Therefore, the excitability threshold for the second pulse is slightly higher and, although the feedback is strong enough to cross this threshold, the pulse is slightly delayed. Thus, the distance between the two TLSs increases, resulting in an effectively repulsive interaction. We note that since the interaction is mediated by a slow variable recovery, the pulses interact almost exclusively forward in time. Such non-reciprocal interactions are typical for time-delayed systems. For instance, Ref. [51] discusses non-reciprocal interaction between TLSs in a type I excitable system based on the delayed Adler model.

The results of this subsection assuming a slow RTD – the stable TLS branch coexisting with the excitable, stable steady state, repulsive TLS interactions, and even the winged shape of the TLS branches – are qualitatively strikingly similar to the simple delayed FHN neuron model of an RTD-LD studied in Ref. [63]. There it was shown that the n pulses in a TLS$_n$ can be manipulated independently and may thus serve as memory. We can conclude that the approximation of using the FHN model in Ref. [63] is justified to qualitatively reproduce the pulse dynamics in the adiabatic limit of a slow RTD. Moreover, TLSs are suitable to act as memory in the RTD-LD because of their robustness to perturbations, called self-healing, and their repulsive interaction, which allows to store information over long periods of time.

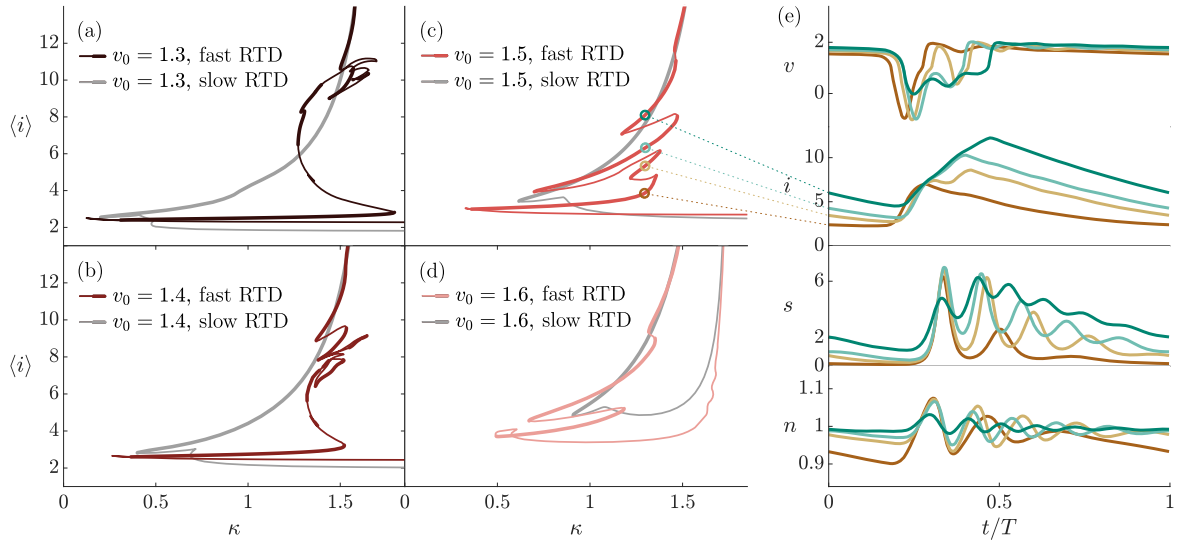

Figure 4.5: (a)-(d) Continuation of TLS_1 in the feedback strength κ for different bias voltages v_0 in the fast (shades of red) and slow (gray, cf. Fig. 4.2) RTD regimes. (e) Time traces of the multistable TLS solution at $v_0 = 1.5$ and $\kappa = 1.3$.

4.3 Regime of the fast RTD

Now, we consider the scenario where the RTD and the laser evolve on similar time scales by setting the characteristic time scale of the RTD to $t_{\mathrm{c,fast}} = t_{\mathrm{c,slow}}/1000$, cf. Section 3.5. A fast RTD means that the adiabatic approximation from Section 3.4 used in Section 4.2 is no longer justified and we have to consider the complete RTD-LD system (3.1)-(3.4). In this scenario, we anticipate the time scale of the laser relaxation oscillations to interact with the RTD spiking period.

Figure 4.5 shows a continuation in the feedback strength κ, along with the branches from Fig. 4.2 for a slow RTD in gray. Panels (a) to (d) are slices at different bias voltages $v_0 \in \{1.3, 1.4, 1.5, 1.6\}$ in the PDC II region. As in Fig. 4.2, the TLSs exist and are stable above a threshold in κ that is similar to the slow-RTD scenario for $v_0 \in \{1.3, 1.4\}$, but the onset is lower for $v_0 \in \{1.5, 1.6\}$. Time simulations confirm that the TLSs arise due to excitability of the steady state, just as in the slow-RTD regime. Furthermore, the large-scale behavior of the branches is similar with respect to the resonance catastrophe, where the branches diverge to infinite energy at $\kappa = 1.5$. However, the laser dynamics lead to much more intricate branches, which can be attributed to relaxation oscillations of the laser.

The most striking difference between the fast-RTD and slow-RTD regime is that the branch is monostable from $\kappa = 0.3$ to $\kappa = 0.7$ but distorts into a number of multistable patches around $\kappa = 1.5$, whereas the slow RTD branch has a single monotonous stable patch. To illustrate the significance of the multistable periodic solutions, panel (e) compares the time traces of four exemplary TLS solutions of different energy coexisting at the same bias voltage $v_0 = 1.5$ and feedback strength $\kappa = 1.3$. The multistability of the TLSs is particularly interesting because it could enable nonbinary encoding. Yet the four solutions have slightly different periods, $T \in \{22.86, 22.34, 22.13, 22.08\}$, which implies that they move at different speed around the circuit, rendering nonbinary encoding unstable.

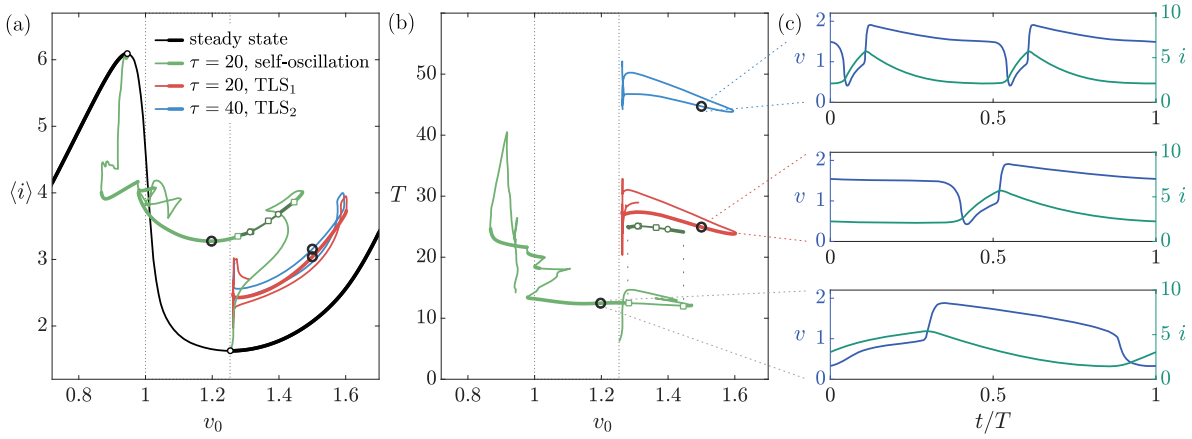

Figure 4.6: (a) Continuation in the bias voltage v_0 at $\kappa = 0.5$ in the fast-RTD regime. The steady state (black) loses its stability through two AH bifurcations (white circles). The green, red, and blue branches correspond to the periodic self-oscillation, TLS$_1$, and TLS$_2$, respectively. (b) Period T of the periodic branches. The dark green branch arises through a period-doubling (white squares) of the self-oscillation. (c) Exemplary time traces in voltage v and current i of the solutions at $v_0 = 1.2$ for self-oscillation and $v_0 = 1.5$ for the TLS$_1$ and TLS$_2$. The position of the time traces in (a) and (b) is indicated by black circles.

A continuation in the bias voltage v_0 at fixed $\kappa = 0.5$, as shown in Fig. 4.6, reveals crucial differences to the analogous Fig. 4.3 for a slow RTD. In panel (a), the self-oscillation branch (green) connects to the steady state (black) at two AH bifurcations (white circles) and is much more twisted, including an intricate multistable region near $v_0 = 1$. Further, the TLS$_1$ (red) and TLS$_2$ (blue) branches attach to the canard explosion of the self-oscillation branch. This reordering of where the branches attach can be explained by shorter pulse widths, which reduce finite domain size effects. Furthermore, around $v_0 = 1.3$ and $v_0 = 1.5$, the self-

oscillation branch loses stability in two period-doubling (PD) bifurcations (white squares), between which the emerging branch in dark green (whose period is indeed twice as large, see panel (b)) itself loses stability in a pair of AH bifurcations, followed by another pair of PD bifurcations. However, the spectrum of Floquet multipliers shows that solution at about $v_0 > 1.26$ is only marginally stable; a manual continuation with time simulations jumps to TLS_1 or the steady state branch. Note that the period T of the self-oscillation in panel (b) is generally similar to the solution without feedback presented in Fig. 4.1, i.e., convex with unstable legs downward near the boundary of the NDC region. We do not see this shape in the analogous Fig. 4.3, again due to finite-size effects. The striking observation in this figure, however, is that while the TLS_1 branch is stable for a wide range of v_0, the TLS_2 branch is entirely unstable. Panel (b) illustrates that, while the self-oscillation branch is independent of the delay T, the TLS branches have a period $T = \tau + \delta$ that changes with the delay through a shorter or longer resting time while the pulse remains the same. The exemplary time traces of the periodic solutions at $v_0 = 1.5$ in panel (c) demonstrate that the TLSs are indeed localized perturbations to a background resting state, but their qualitative shape remains mostly the same, whereas the self-oscillation fills the whole temporal domain.

The question that remains is why the TLS_2 branch is unstable. By initializing two non-equidistant pulses at a distance $d_0 = 0.4\tau \approx 0.376T$ in local time σ, we find in Fig. 4.7 (a) that the two respective pulses in the carrier number n move closer and closer over time until they eventually merge at about $t = 1800$. The two-time representation of this transition for the current i in panel (b) reveals how the pulses interact as they race around the RTD-LD circuit. We conclude that the interaction of the pulses is *attractive*. Consequently, the branch of the equidistant TLS_2 solution in Fig. 4.5 is unstable due to this attractive interaction between the pulses.

Notably in Fig. 4.7 (a), the second of the two spikes has a higher peak intensity, as shown in the inset. The difference in the peak height holds the key to understanding the mechanism by which the pulses attract each other. The second pulse occurs while the the carrier number n of the first pulse has not yet fully relaxed. Consequently, the second pulse has more gain and is more intense than the first. Since the higher intensity leads to stronger feedback on the voltage v, the excitable response is slightly accelerated and thus, the second pulse catches up with the first. This mechanism occurs because the slow variable that governs the pulse

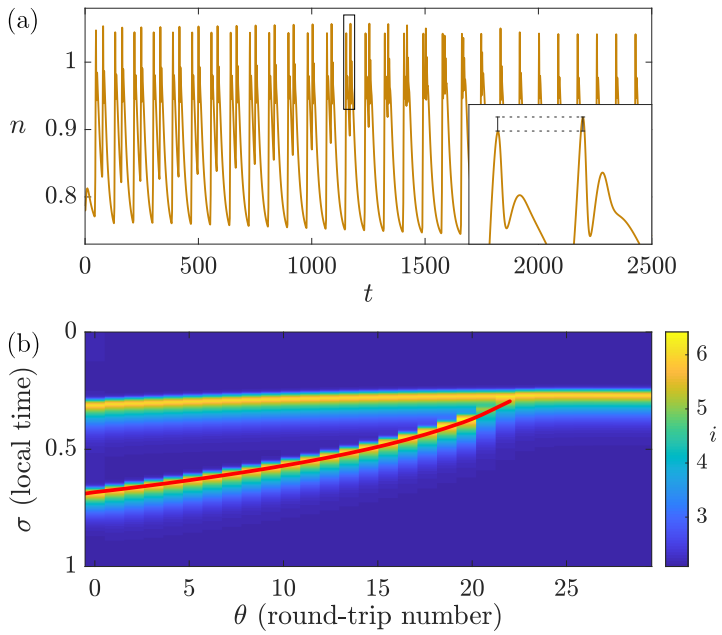

Figure 4.7: (a) Time series of the carrier number n of the TLS_2 at $v_0 = 1.5$, $\kappa = 1$, and $\tau = 80$ in the fast-RTD regime. The inset of one period shows that the second pulse is larger than the first. (b) The corresponding two-time diagram of two TLSs generated from an initial condition with a pair of spikes spaced a distance $d_0 = 0.4\tau \approx 0.376T$ apart in local time σ. The folding factor is $T = \tau + \delta_2 \approx 85.09$. The fit (red line) of the position of the second pulse with fit parameter $(50.3 \pm 0.3) \cdot 10^{-3}$ corresponds to the solution of the equation of motion (4.8).

interaction is the carrier number n, which effectively *decreases* the excitability threshold in the feedback strength of a pulse. For the slow RTD, on the contrary, the incomplete recovery of the current i *increases* the excitability threshold.

Let us now derive equations of motion for the pulse interaction from the simple ansatz that the interaction forces decay exponentially – motivated by the exponential decay of the carrier number n in the pulse tail with rate t_n – and act only forward in time because of causality. We seek to model TLSs moving in the parameter space (θ, σ) of the two-time diagram in Fig. 4.7 in the fast-RTD scenario. The TLSs live on a helical quasi-torus, where their position is defined by the angle $2\pi\sigma$ and the length θ. Let us assume for concreteness just two interacting TLSs S_1 and S_2; The generalization to multiple TLSs is straightforward. Further, since the local time σ corresponds to the position on the optical delay line of the RTD-LD circuit, it is reasonable to suppose that the interaction forces between the TLSs do not depend explicitly on the round-trip number θ but only on the distance $|\sigma_2 - \sigma_1|$ and their

ordering in local time. Without loss of generality, assume $\sigma_2 > \sigma_1$.

In general, there can be a "force" forward, F_+, and backward, F_-, in local time so that

$$\begin{aligned} \frac{\mathrm{d}\sigma_1}{\mathrm{d}\theta} &= F_-(\sigma_1 - \sigma_2 + 1) + F_+(\sigma_1 - \sigma_2 + 1)\,, \\ \frac{\mathrm{d}\sigma_2}{\mathrm{d}\theta} &= F_-(\sigma_2 - \sigma_1) + F_+(\sigma_2 - \sigma_1)\,, \end{aligned} \tag{4.1}$$

where adding the period 1 in the expression for $\mathrm{d}\sigma_1/\mathrm{d}\theta$ accounts for the correct ordering, for S_2 can only affect S_1 on the next round trip (since causality rules out interaction backward in time t). Note that F_- and F_+ are viscous forces because they are proportional to a velocity in the two-time representation rather than an acceleration as is typical of TLSs [41, 75, 51].

Assuming an exponential decay with distance because the mechanism of attraction is explained by the slope of the carrier number n (cf. Section 4.3), the equations of motion are

$$\begin{aligned} \frac{\mathrm{d}\sigma_1}{\mathrm{d}\theta} &= -A_- \exp(-\gamma_-(\sigma_1 - \sigma_2 + 1)T) \\ &\quad + A_+ \exp(-\gamma_+(\sigma_1 - \sigma_2 + 1)T)\,, \\ \frac{\mathrm{d}\sigma_2}{\mathrm{d}\theta} &= -A_- \exp(-\gamma_-(\sigma_2 - \sigma_1)T) \\ &\quad + A_+ \exp(-\gamma_+(\sigma_2 - \sigma_1)T)\,, \end{aligned} \tag{4.2}$$

where $A_\pm$ is the strength of the interaction force that contains the overlap integrals between the corresponding (adjoint) Goldstone modes and the tail of the interacting pulses. Moreover, we can simplify matters by noting that the attraction forward in time is negligible ($A_+ \ll A_-$) because the tail of the carrier number is small to the left. Thus, the TLSs move only backward in local time

$$\begin{aligned} \frac{\mathrm{d}\sigma_1}{\mathrm{d}\theta} &= -A_- \exp(-\gamma_-(\sigma_1 - \sigma_2 + 1))\,, \\ \frac{\mathrm{d}\sigma_2}{\mathrm{d}\theta} &= -A_- \exp(-\gamma_-(\sigma_2 - \sigma_1))\,. \end{aligned} \tag{4.3}$$

This tail in n decays exponentially with the rate

$$\gamma_- = \gamma_\mathrm{l} + \gamma_\mathrm{m} + \gamma_\mathrm{nr} \tag{4.4}$$

to the off-state of the laser after a light pulse. The minus sign as index is omitted in the

following.

The evolution of the difference $d = \sigma_2 - \sigma_1$ is therefore

$$\begin{aligned}\frac{\mathrm{d}d}{\mathrm{d}\theta} &= -A[\exp(-\gamma d T) - \exp(\gamma(d-1)T)] \\ &= -A\exp(-\gamma T/2)[\exp(-\gamma(d-1/2)T) \\ &\qquad\qquad - \exp(\gamma(d-1/2)T)] \\ &= 2A\exp(-\gamma T/2)\sinh(\gamma(d-1/2)T)\,, \end{aligned} \tag{4.5}$$

which proves that the equilibrium occurs at $d = 1/2$. To solve differential equation Eq. (4.5), we substitute $D = \gamma(d-1/2)T$ or equivalently $d = D/(\gamma T) + 1/2$ to arrive at

$$\begin{aligned}\frac{\mathrm{d}D}{\mathrm{d}\theta} &= 2A\gamma T\exp(-\gamma T/2)\sinh(D) \\ &= B\sinh(D) \end{aligned} \tag{4.6}$$

with $B = 2A\gamma T\exp(-\gamma T/2)$. Finally, we separate the variables and integrate,

$$\begin{aligned}&\frac{1}{B}\int_{D_0}^{D}\mathrm{d}\tilde{D}\,\frac{1}{\sinh(\tilde{D})} = \int_0^{\theta}\mathrm{d}\vartheta\; = \theta \\ \Leftrightarrow\quad &\log\left(\frac{\tanh(D/2)}{\tanh(D_0/2)}\right) = B\theta \\ \Leftrightarrow\quad &D = 2\,\mathrm{arctanh}\left(\mathrm{e}^{B\theta}\tanh(D_0/2)\right). \end{aligned} \tag{4.7}$$

Resubstituting d for D and recalling that $\gamma = 1/t_\mathrm{n}$, we arrive at the solution

$$d(\theta) = \frac{1}{2} + 2\frac{t_\mathrm{n}}{T}\,\mathrm{arctanh}\left(\mathrm{e}^{B\theta}\tanh\left(\frac{T}{2t_\mathrm{n}}\left[d_0 - \frac{1}{2}\right]\right)\right), \tag{4.8}$$

with the fit parameter $B = 2A\exp\left(-\frac{T}{2t_\mathrm{n}}\right)\frac{T}{t_\mathrm{n}}$. A fit based on Eq. (4.8), represented by the red line in Fig. 4.7 (b), yields $B = (50.3 \pm 0.3)\cdot 10^{-3}$ and is in excellent agreement with the time simulation.

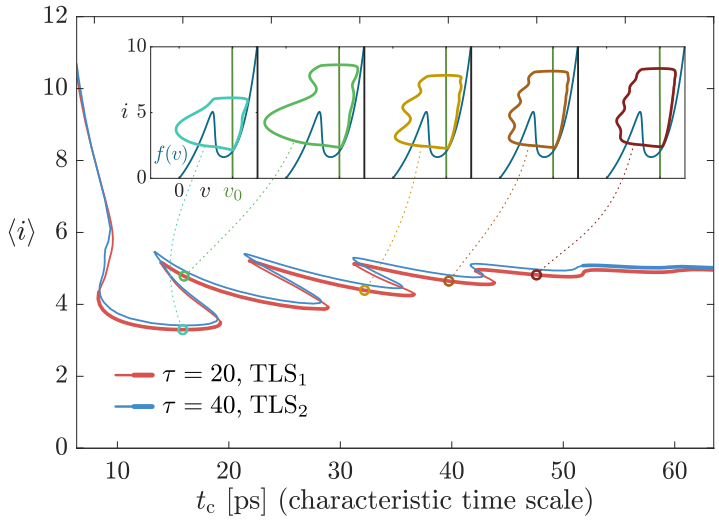

Figure 4.8: Continuation of the TLS$_1$ and TLS$_2$ solutions in the characteristic time scale t_c at $v_0 = 1.5$ and $\kappa = 1$. The slow-RTD scenario is located at $t_c = 15.9\,\text{ns}$, the fast-RTD scenario at $t_c = 15.9\,\text{ps}$.

4.4 Characteristic time scale

Having discussed the similarities and differences between the slow and the fast RTD, we finally consider the bifurcation diagram of the TLS$_1$ and TLS$_2$ solutions in the characteristic time scale t_c shown in Fig. 4.8 to explain how these two regimes are related. In this diagram, the fast-RTD time scale corresponds to $t_c = 15.9\,\text{ps}$ and the slow RTD is located far to the right at $t_c = 15.9\,\text{ns}$ in the adiabatic limit (the branch remains relatively constant beyond $t_c = 60\,\text{ps}$). There are two key features of the TLS solutions that we saw above to point out here.

First, the TLS$_2$ loses stability at around $t_c = 52\,\text{ps}$ and remains unstable for smaller characteristic time scales. This is the point where the pulse interaction forces change. Apart from the difference in stability, the TLS$_1$ and the TLS$_2$ branch agree well even quantitatively.

Second, both TLS branches exhibit slanted snaking in the fast-RTD domain, where the stability of the TLS$_2$ breaks down. Notably, the stable patches of the snaking correspond to those of the continuation in κ in Fig. 4.5. This horizontal snaking is another consequence of the complex laser dynamics. The insets in Fig. 4.8 of stable periodic solutions in the (v, i)-phase-space show that the stable patches evidently correspond to different numbers of oscillations in the tail, which appear as bumps in the phase space trajectory, first one (cyan), then two, etc., up to five (brown). Note that the multistable solutions of the branches

at $\kappa = 1$ and $v_0 = 1.5$ are exactly those two stable solutions from Fig. 4.5 (c) at $\kappa = 1$. Consequently, the multistability we discussed above has its origin in the snaking of the TLS_1 branch in the characteristic time scale. However, with even stronger feedback, the snaking branches separate into islands, which further indicates that the dynamics of the RTD-LD are considerably convoluted.

5 Conclusions

Our investigation of the RTD-LD system with time-delayed feedback demonstrates with a realistic model derived from Ref. [57] that this optoelectronic circuit is indeed excitable and functions as an artificial neuron by generating temporally localized states (TLSs), which can serve as memory in neuromorphic computing. The simpler delayed FitzHugh–Nagumo (FHN) model [63] previously used to model the RTD-LD adequately describes the qualitative dynamics if the RTD is slow compared to the laser. In the slow-RTD limit, we find repulsive TLS interaction, which makes the memory stable. Yet our analysis has unveiled novel features and challenges, including the multistability of TLSs and repulsive TLS interaction, if the RTD is fast, i.e., on a similar time scale as the laser. Although multistability could, in principle, enable nonbinary encoding, the periods of the coexisting TLSs types are not the same. Furthermore, the attractive interaction, which we could explain by the dynamics of the carrier number of the laser and describe analytically with excellent agreement, makes memory in the fast-RTD regime impossible, except for large delays. The importance of the laser dynamics is exemplified by the complex bifurcation scenarios with a fast RTD. We find a transition between the slow-RTD and fast-RTD regime through slanted snaking in the characteristic time scale of the RTD.

Although our bifurcation analysis aims to provide a comprehensive understanding of how the more realistic model presented here agrees with or differs from simpler approximate models like the FHN model, numerical path continuation of the system proves very difficult. The self-oscillation branch serves to show the immense complexity introduced by the laser dynamics. We focus here on the relevant parts for understanding, but there is more to explore in the RTD-LD system.

In particular, it would be interesting to investigate which bifurcations connect the two

regimes of the RTD time scale with different TLS interaction mechanism. Let us emphasize here that the RTD-LD is numerically challenging to analyze; since every eigenvalue crossing the stability threshold results in another branch emerging, the full complexity of the RTD-LD model, including all unstable branches, is daunting and not necessarily enlightening. An interesting variation could be a smaller laser, which might yield higher speeds, but would require to address the increased noise through Fokker-Planck equations as was already done for the FHN system [37]. The prospect of experimental realization, taking into account the theoretical findings in this paper, with all its caveats, stands as a promising research project to show that the RTD-LD might work in practice as an artificial neuron for neuromorphic computing.

A System parameters

The system parameters are listed in Table 2 along with typical values in the numerical implementation. Most fixed values are consistent with those in Ref. [57], but we have chosen a different value for d to avoid a discontinuity in the current-voltage characteristic $f(v)$.

Table 2: Overview of the model parameters and their typical values. Parameters that apply only to the non-dimensionalized system are highlighted in purple.

	RTD parameters	**value**
a	$f(V)$ parameter	$-5.5 \cdot 10^{-5}$ A
b	$f(V)$ parameter	0.033 V
c	$f(V)$ parameter	0.113 V
d	$f(V)$ parameter	$-3 \cdot 10^{-3}$ V
n_1	$f(V)$ parameter	0.185
n_2	$f(V)$ parameter	0.045
h	$f(V)$ parameter	$18 \cdot 10^{-5}$ A
κ	optical feedback rate (LD→RTD)	varied
κ		varied
R	resistance	10 Ω
r		$9.0 \cdot 10^{-4}$
C	capacitance	2 {nF, fF}
L	inductance	126 {µH, nH}
V_0	DC bias voltage	varied
v_0		varied
σ	electrical noise amplitude	0
	LD parameters	
N_0	transparency carrier number	$5 \cdot 10^5$
n_0		2.5
α	polarization factor	0
τ_s	photon lifetime	$5 \cdot 10^{-13}$ s
τ_n	carrier lifetime	$3.3 \cdot 10^{-10}$ s
γ_m	Spont. em. into lasing mode	10^7 s^{-1}
γ_l	Spont. em. into leaky modes	10^9 s^{-1}
γ_{nr}	non-radiative recombination	$2 \cdot 10^9$ s^{-1}
η	current injection efficiency (RTD→LD)	1
η		0.57
J	bias current in laser	200 µA
j		−0.43
τ	time delay of light coupling (LD→RTD)	{0.32, 0.63} ns
τ		{20, 40}
	derived parameters	
β	spont. em. coupling $\beta = \gamma_m/(\gamma_m + \gamma_l)$	0.01
J_{th}	transcritical bifurcation value	338 µA
j_{th}		1
μ^2	stiffness	1.96
t_c	characteristic time scale of RTD	15.9 {ns, ps}
	physical constants	
q_e	elementary charge	$1.60 \cdot 10^{-19}$ C
k_B	Boltzmann constant	$1.38 \cdot 10^{-23}$ $\frac{J}{K}$
T	temperature	300 K

References

[1] F. T. Arecchi, G. Giacomelli, A. Lapucci, and R. Meucci. Two-dimensional representation of a delayed dynamical system. *Physical Review A*, 45(7):R4225–R4228, Apr. 1992. doi:0.1103/PhysRevA.45.R4225.

[2] J. Argyris, G. Faust, M. Haase, and R. Friedrich. *An Exploration of Dynamical Systems and Chaos*. Springer, Berlin, Heidelberg, Apr. 2015. ISBN 9783662460429. doi:10.1007/978-3-662-46042-9.

[3] A. Bacci, J. R. Huguenard, and D. A. Prince. Functional autaptic neurotransmission in fast-spiking interneurons: A novel form of feedback inhibition in the neocortex. *Journal of Neuroscience*, 23(3):859–866, Feb. 2003. doi:10.1523/JNEUROSCI.23-03-00859.2003.

[4] B. V. Benjamin, P. Gao, E. McQuinn, S. Choudhary, A. R. Chandrasekaran, J.-M. Bussat, R. Alvarez-Icaza, J. V. Arthur, P. A. Merolla, and K. Boahen. Neurogrid: A mixed-analog-digital multichip system for large-scale neural simulations. *Proceedings of the IEEE*, 102 (5):699–716, May 2014. doi:10.1109/JPROC.2014.2313565.

[5] E. Benoît, J. F. Callot, F. Diener, and M. Diener. Chasse au canard. *Collectanea Mathematica*, 31-32:37–119, 1981.

[6] K. B. Blyuss and Y. N. Kyrychko. Sex, ducks, and rock 'n' roll: Mathematical model of sexual response. *Chaos: An Interdisciplinary Journal of Nonlinear Science*, 33(4):043106, May 2023. doi:10.1063/5.0143190.

[7] D. Brunner, B. Penkovsky, R. Levchenko, E. Schöll, L. Larger, and Y. Maistrenko. Two-dimensional spatiotemporal complexity in dual-delayed nonlinear feedback systems: Chimeras and dissipative solitons. *Chaos: An Interdisciplinary Journal of Nonlinear Science*, 28(10):103106, Oct. 2018. doi:10.1063/1.5043391.

[8] A. V. Bukh, I. A. Shepelev, E. M. Elizarov, S. S. Muni, E. Schöll, and G. I. Strelkova. Role of coupling delay in oscillatory activity in autonomous networks of excitable neurons with dissipation. *Chaos: An Interdisciplinary Journal of Nonlinear Science*, 33(7):073114, July 2023. doi:10.1063/5.0147883.

[9] H. J. Caulfield and S. Dolev. Why future supercomputing requires optics. *Nature Photonics*, 4(5):261–263, May 2010. doi:10.1038/nphoton.2010.94.

[10] L. L. Chang, L. Esaki, and R. Tsu. Resonant tunneling in semiconductor double barriers. *Applied Physics Letters*, 24(12):593–595, June 1974. doi:10.1063/1.1655067.

[11] W. Coomans, L. Gelens, S. Beri, J. Danckaert, and G. Van der Sande. Solitary and coupled semiconductor ring lasers as optical spiking neurons. *Physical Review E*, 84(3):036209, Sept. 2011. doi:10.1103/physreve.84.036209.

[12] H. P. Cowley, M. Natter, K. Gray-Roncal, R. E. Rhodes, E. C. Johnson, N. Drenkow, T. M. Shead, F. S. Chance, B. Wester, and W. Gray-Roncal. A framework for rigorous evaluation of human performance in human and machine learning comparison studies. *Scientific Reports*, 12(1):5444, Mar. 2022. doi:10.1038/s41598-022-08078-3.

[13] M. Desroches, M. Krupa, and S. Rodrigues. Inflection, canards and excitability threshold in neuronal models. *Journal of Mathematical Biology*, 67(4):989–1017, Oct. 2013. doi:10.1007/s00285-012-0576-z.

[14] K. Engelborghs, T. Luzyanina, and D. Roose. Numerical bifurcation analysis of delay differential equations using DDE-BIFTOOL. *ACM Transactions on Mathematical Software*, 28(1):1–21, Mar. 2002. doi:10.1145/513001.513002.

[15] T. Erneux. *Applied Delay Differential Equations*, volume 3 of *Surveys and Tutorials in the Applied Mathematical Sciences*. Springer, New York, 1 edition, Mar. 2009. ISBN 9780387743721. doi:10.1007/978-0-387-74372-1.

[16] T. Ferreira de Lima, B. J. Shastri, A. N. Tait, M. A. Nahmias, and P. R. Prucnal. Progress in neuromorphic photonics. *Nanophotonics*, 6(3):577–599, Mar. 2017. doi:10.1515/nanoph-2016-0139.

[17] R. FitzHugh. Impulses and physiological states in theoretical models of nerve membrane. *Biophysical Journal*, 1(6):445–466, July 1961. doi:10.1016/S0006-3495(61)86902-6.

[18] C. Freitag, M. Berners-Lee, K. Widdicks, B. Knowles, G. S. Blair, and A. Friday. The real

climate and transformative impact of ict: A critique of estimates, trends, and regulations. *Patterns*, 2(9):100340, Sept. 2021. doi:10.1016/j.patter.2021.100340.

[19] S. B. Furber, F. Galluppi, S. Temple, and L. A. Plana. The SpiNNaker project. *Proceedings of the IEEE*, 102(5):652–665, May 2014. doi:10.1109/JPROC.2014.2304638.

[20] B. Garbin, J. Javaloyes, G. Tissoni, and S. Barland. Topological solitons as addressable phase bits in a driven laser. *Nature Communications*, 6(1):5915, Jan. 2015. doi:10.1038/ncomms6915.

[21] W. Gerstner and W. M. Kistler. *Spiking Neuron Models: Single Neurons, Populations, Plasticity*. Cambridge University Press, Cambridge, 1 edition, Aug. 2002. ISBN 9780521890793. doi:10.1017/CBO9780511815706.

[22] G. Giacomelli and A. Politi. Relationship between delayed and spatially extended dynamical systems. *Physical Review Letters*, 76(15):2686–2689, Apr. 1996. doi:10.1103/PhysRevLett.76.2686.

[23] G. Girier, M. Desroches, and S. Rodrigues. From integrator to resonator neurons: A multiple-timescale scenario. *Nonlinear Dynamics*, 111(17):16545–16556, Sept. 2023. doi:10.1007/s11071-023-08687-1.

[24] D. M. Grobman. O gomeomorfizme sistem differencial'nych uravnenij. *Doklady Akademii Nauk SSSR*, 128(5):880–881, 1959.

[25] D. Guo, S. Wu, M. Chen, M. Perc, Y. Zhang, J. Ma, Y. Cui, P. Xu, Y. Xia, and D. Yao. Regulation of irregular neuronal firing by autaptic transmission. *Scientific Reports*, 6(1): 26096, May 2016. doi:10.1038/srep26096.

[26] J. K. Hale and S. M. V. Lunel. *Introduction to Functional Differential Equations*, volume 99 of *Applied Mathematical Sciences*. Springer, New York, 1 edition, Oct. 1993. ISBN 9781461287414. doi:10.1007/978-1-4612-4342-7.

[27] P. Hartman. A lemma in the theory of structural stability of differential equations. *Proceedings of the American Mathematical Society*, 11(4):610–620, Apr. 1960. doi:10.1090/S0002-9939-1960-0121542-7.

[28] P. Hartman. On local homeomorphisms of Euclidean spaces. *Boletín de la Sociedad Matemática Mexicana*, 5(2):220–241, 1960.

[29] M. Hejda, J. Robertson, J. Bueno, J. A. Alanis, and A. Hurtado. Neuromorphic encoding of image pixel data into rate-coded optical spike trains with a photonic VCSEL-neuron. *APL Photonics*, 6(6):060802, June 2021. doi:10.1063/5.0048674.

[30] M. T. Hill and M. C. Gather. Advances in small lasers. *Nature Photonics*, 8(12):908–918, Nov. 2014. doi:10.1038/nphoton.2014.239.

[31] M. E. Hobart and Z. S. Schiffman. *Information Ages: Literacy, Numeracy, and the Computer Revolution*. John Hopkins University Press, Baltimore, 1 edition, May 2000. ISBN 9780801864124. URL https://dl.acm.org/doi/10.5555/552440.

[32] A. L. Hodgkin and A. F. Huxley. A quantitative description of membrane current and its application to conduction and excitation in nerve. *The Journal of Physiology*, 117(4): 500, Aug. 1952. doi:10.1113/jphysiol.1952.sp004764.

[33] E. M. Izhikevich. Neural excitability, spiking and bursting. *International Journal of Bifurcation and Chaos*, 10(6):1171–1266, June 1999. doi:10.1142/S0218127400000840.

[34] E. M. Izhikevich. *Dynamical Systems in Neuroscience: The Geometry of Excitability and Bursting*. MIT Press, Cambridge, London, 1st edition, 2007. ISBN 9780262090438. doi:10.7551/mitpress/2526.001.0001.

[35] E. M. Izhikevich and R. FitzHugh. FitzHugh-Nagumo model. *Scholarpedia*, 1(9):1349, Sept. 2006. doi:10.4249/scholarpedia.1349. revision #123664.

[36] L. Kuhnert, K. I. Agladze, and V. I. Krinsky. Image processing using light-sensitive chemical waves. *Nature*, 337(6204):244–247, Jan. 1989. doi:10.1038/337244a0.

[37] B. Lindner, J. García-Ojalvo, A. Neiman, and L. Schimansky-Geier. Effects of noise in excitable systems. *Physics Reports*, 392(6):321–424, Mar. 2004. doi:10.1016/j.physrep.2003.10.015.

[38] A. Lorents, M.-E. Colin, I. E. Bjerke, S. Nougaret, L. Montelisciani, M. Diaz, P. Verschure, and J. Vezoli. Human Brain Project partnering projects meeting: Status quo and outlook. *eNeuro*, 10(9), Sept. 2023. doi:10.1523/ENEURO.0091-23.2023.

[39] E. N. Lorenz. Deterministic nonperiodic flow. *Journal of the Atmospheric Sciences*, 20(2): 130–141, Mar. 1963. doi:10.1175/1520-0469(1963)020<0130:DNF>2.0.CO;2.

[40] R.-M. Ma and R. F. Oulton. Applications of nanolasers. *Nature Nanotechnology*, 14(1): 12–22, Jan. 2019. doi:10.1038/s41565-018-0320-y.

[41] T. Maggipinto, M. Brambilla, G. K. Harkness, and W. J. Firth. Cavity solitons in semiconductor microresonators: Existence, stability, and dynamical properties. *Physical Review E*, 62(6):8726–8739, Dec. 2000. doi:10.1103/PhysRevE.62.8726.

[42] F. Marino and G. Giacomelli. Spatiotemporal description of long-delayed systems: Ruling the dynamics. *Physical Review E*, 98(6):060201, Dec. 2018. doi:10.1103/PhysRevE.98.060201.

[43] F. Marino and G. Giacomelli. Excitable wave patterns in temporal systems with two long delays and their observation in a semiconductor laser experiment. *Physical Review Letters*, 122(17):174102, May 2019. doi:10.1103/PhysRevLett.122.174102.

[44] D. Marković, A. Mizrahi, D. Querlioz, and J. Grollier. Physics for neuromorphic computing. *Nature Reviews Physics*, 2(9):499–510, Sept. 2020. doi:10.1038/s42254-020-0208-2.

[45] H. Markram. The Human Brain Project. *Scientific American*, 306(6):50–55, June 2012. URL `http://www.jstor.org/stable/26014516`.

[46] J. Mayer Martins, S. V. Gurevich, and J. Javaloyes. Excitability and memory in a time-delayed optoelectronic neuron. *arXiv:2402.00227*, Jan. 2024. doi:10.48550/arXiv.2402.00227.

[47] J. Mayer Martins, S. V. Gurevich, and J. Javaloyes. Supplementary material. *Zenodo*, Feb. 2024. doi:10.5281/zenodo.10601669.

[48] P. A. Merolla, J. V. Arthur, R. Alvarez-Icaza, A. S. Cassidy, J. Sawada, F. Akopyan, B. L. Jackson, N. Imam, C. Guo, Y. Nakamura, B. Brezzo, I. Vo, S. K. Esser, R. Appuswamy,

B. Taba, A. Amir, M. D. Flickner, W. P. Risk, R. Manohar, and D. S. Modha. A million spiking-neuron integrated circuit with a scalable communication network and interface. *Science*, 345(6197):668–673, Aug. 2014. doi:10.1126/science.1254642.

[49] D. A. B. Miller. Attojoule optoelectronics for low-energy information processing and communications. *Journal of Lightwave Technology*, 35(3):346–396, Feb. 2017. doi:10.1109/JLT.2017.2647779.

[50] C. Morris and H. Lecar. Voltage oscillations in the barnacle giant muscle fiber. *Biophysical Journal*, 35(1):193–213, July 1981. doi:10.1016/s0006-3495(81)84782-0.

[51] L. Munsberg, J. Javaloyes, and S. V. Gurevich. Topological localized states in the time delayed Adler model. *Chaos: An Interdisciplinary Journal of Nonlinear Science*, 30(6):063137, June 2020. doi:10.1063/5.0002015.

[52] J. D. Murray. *Mathematical Biology I: An Introduction*, volume 17 of *Interdisciplinary Applied Mathematics*. Springer, New York, 3 edition, June 2002. ISBN 978-0-387-95223-9. doi:10.1007/b98868.

[53] J. D. Murray. *Mathematical Biology II: Spatial Models and Biomedical Applications*, volume 18 of *Interdisciplinary Applied Mathematics*. Springer, New York, 3 edition, Jan. 2003. ISBN 978-0-387-95228-4. doi:10.1007/b98868.

[54] J. Nagumo, S. Arimoto, and S. Yoshizawa. An active pulse transmission line simulating nerve axon. *Proceedings of the IEEE*, 50(10):2061–2070, Oct. 1962. doi:10.1109/JRPROC.1962.288235.

[55] B. Øksendal. *Stochastic Differential Equations: An Introduction with Applications*. Springer Nature, Berlin, Heidelberg, 5 edition, Mar. 2003. ISBN 9783662036204. doi:10.1007/978-3-642-14394-6.

[56] I. Ortega-Piwonka, O. Piro, J. Figueiredo, B. Romeira, and J. Javaloyes. Bursting and excitability in neuromorphic resonant tunneling diodes. *Physical Review Applied*, 15(3): 034017, Mar. 2021. doi:10.1103/PhysRevApplied.15.034017.

[57] I. Ortega-Piwonka, M. Hejda, J. Alanis, J. ao Lourenço, A. Hurtado, J. Figueiredo, B. Romeira, and J. Javaloyes. Spike propagation in a nanolaser-based optoelectronic neuron. *Optical Materials Express*, 12(7):2679–2696, July 2022. doi:10.1364/OME.451706.

[58] F. Pedaci, Z. Huang, M. van Oene, S. Barland, and N. H. Dekker. Excitable particles in an optical torque wrench. *Nature Physics*, 7(3):259–264, Mar. 2011. doi:10.1038/nphys1862.

[59] S. A. Prescott. *Encyclopedia of Computational Neuroscience*, chapter Excitability: Types I, II, and III, pages 1158–1164. Springer, New York, 1 edition, Mar. 2015. ISBN 978-1-4614-6674-1. URL https://doi.org/10.1007/978-1-4614-6675-8_151.

[60] K. Pyragas. Continuous control of chaos by self-controlling feedback. *Physics Letters A*, 170(6):421–428, Nov. 1992. doi:10.1016/0375-9601(92)90745-8.

[61] Z. Qu, G. Hu, A. Garfinkel, and J. N. Weiss. Nonlinear and stochastic dynamics in the heart. *Physics Reports*, 543(2):61–162, Oct. 2014. doi:10.1016/j.physrep.2014.05.002.

[62] B. Romeira and A. Fiore. Purcell effect in the stimulated and spontaneous emission rates of nanoscale semiconductor lasers. *IEEE Journal of Quantum Electronics*, 54(2):1–12, Apr. 2018. doi:10.1109/JQE.2018.2802464.

[63] B. Romeira, R. Avó, J. M. L. Figueiredo, S. Barland, and J. Javaloyes. Regenerative memory in time-delayed neuromorphic photonicresonators. *Scientific Reports*, 6(1):19510, Jan. 2016. doi:10.1038/srep19510.

[64] B. Romeira, J. M. L. Figueiredo, and J. Javaloyes. Delay dynamics of neuromorphic optoelectronic nanoscale resonators: Perspectives and applications. *Chaos: An Interdisciplinary Journal of Nonlinear Science*, 27(11):114323, Nov. 2017. doi:10.1063/1.5008888.

[65] J. Schemmel, D. Brüderle, A. Grübl, M. Hock, K. Meier, and S. Millner. A wafer-scale neuromorphic hardware system for large-scale neural modeling. In *2010 IEEE International Symposium on Circuits and Systems (ISCAS)*, pages 1947–1950, Paris, Aug. 2010. IEEE. doi:10.1109/ISCAS.2010.5536970.

[66] E. Schöll and H. G. Schuster. *Handbook of Chaos Control*. John Wiley & Sons, Weinheim, 2 edition, Oct. 2007. ISBN 978-3-527-40605-0. doi:10.1002/9783527622313.

[67] J. N. Schulman, H. J. De Los Santos, and D. H. Chow. Physics-based RTD current-voltage equation. *IEEE Electron Device Letters*, 17(5):220–222, May 1996. doi:10.1109/55.491835.

[68] F. Selmi, R. Braive, G. Beaudoin, I. Sagnes, R. Kuszelewicz, and S. Barbay. Relative refractory period in an excitable semiconductor laser. *Physical Review Letters*, 112(18): 183902, May 2014. doi:10.1103/PhysRevLett.112.183902.

[69] B. J. Shastri, M. A. Nahmias, A. N. Tait, A. W. Rodriguez, B. Wu, and P. R. Prucnal. Spike processing with a graphene excitable laser. *Scientific Reports*, 6(1):1–12, Jan. 2016. doi:10.1038/srep19126.

[70] B. J. Shastri, A. N. Tait, T. Ferreira de Lima, W. H. P. Pernice, H. Bhaskaran, C. D. Wright, and P. R. Prucnal. Photonics for artificial intelligence and neuromorphic computing. *Nature Photonics*, 15(2):102–114, Feb. 2021. doi:10.1038/s41566-020-00754-y.

[71] M. Stöhr and M. Wolfrum. Temporal dissipative solitons in the Morris–Lecar model with time-delayed feedback. *Chaos: An Interdisciplinary Journal of Nonlinear Science*, 33 (2):023117, Feb. 2023. doi:10.1063/5.0134815.

[72] S. H. Strogatz. *Nonlinear Dynamics and Chaos: With Applications to Physics, Biology, Chemistry, and Engineering*. CRC Press, Boca Raton, 2 edition, May 2018. ISBN 978-0-8133-4910-7. doi:10.1201/9780429492563.

[73] M. Tlidi, A. G. Vladimirov, and P. Mandel. Interaction and stability of periodic and localized structures in optical bistable systems. *IEEE Journal of Quantum Electronics*, 39 (2):216–226, Jan. 2003. doi:10.1109/JQE.2002.807193.

[74] H. Tsukuma and T. Kubokawa. *Shrinkage Estimation for Mean and Covariance Matrices*. Springer, Singapore, 1 edition, Apr. 2020. ISBN 978-981-15-1596-5.

[75] D. Turaev, A. G. Vladimirov, and S. Zelik. Long-range interaction and synchronization of oscillating dissipative solitons. *Physical Review Letters*, 108(26):263906, June 2012. doi:10.1103/PhysRevLett.108.263906.

[76] M. Van Rossum, W. Schoenmaker, W. Magnus, K. De Meyer, M. D. Croitoru, V. N.

Gladilin, V. M. Fomin, and J. T. Devreese. Moore's law: New playground for quantum physics. *physica status solidi (b)*, 237(1):426–432, Apr. 2003. doi:10.1002/pssb.200301788.

[77] A. G. Vladimirov, J. M. McSloy, D. V. Skryabin, and W. J. Firth. Two-dimensional clusters of solitary structures in driven optical cavities. *Physical Review E*, 65(4):046606, Mar. 2002. doi:10.1103/PhysRevE.65.046606.

[78] J. von Neumann. First draft of a report on the EDVAC. *IEEE Annals of the History of Computing*, 15(4):27–75, 1993. doi:10.1109/85.238389. Unpublished report from 1945.

[79] M. Wechselberger. Canards. *Scholarpedia*, 2(4):1356, Apr. 2007. doi:10.4249/scholarpedia.1356. revision #152256.

[80] S. Wiggins. *Introduction to Applied Nonlinear Dynamical Systems and Chaos*, volume 2 of *Texts in Applied Mathematics*. Springer, New York, 2 edition, Oct. 2003. ISBN 978-0-387-00177-7. doi:10.1007/b97481.

[81] S. Yanchuk and G. Giacomelli. Spatio-temporal phenomena in complex systems with time delays. *Journal of Physics A: Mathematical and Theoretical*, 50(10):103001, Feb. 2017. doi:10.1088/1751-8121/50/10/103001.

[82] S. Yanchuk, S. Ruschel, J. Sieber, and M. Wolfrum. Temporal dissipative solitons in time-delay feedback systems. *Physical Review Letters*, 123(5):053901, July 2019. doi:10.1103/PhysRevLett.123.053901.

[83] A. Zakharova, N. Semenova, V. Anishchenko, and E. Schöll. Time-delayed feedback control of coherence resonance chimeras. *Chaos: An Interdisciplinary Journal of Nonlinear Science*, 27(11):114320, Oct. 2017. doi:10.1063/1.5008385.

[84] Z. Zhao and H. Gu. Transitions between classes of neuronal excitability and bifurcations induced by autapse. *Scientific Reports*, 7(1):6760, July 2017. doi:10.1038/s41598-017-07051-9.